Comput. Methods Appl. Mech. Engrg. 198 (2009) 785–798

Contents lists available at ScienceDirect

Comput. Methods Appl. Mech. Engrg.

journal homepage: www.elsevier.com/locate/cma

Plastic buckling and collapse of thin shell structures, using layered plastic modeling and co-rotational ANDES finite elements

Nélvio Dal Cortivo [a,*], Carlos A. Felippa [b], Henri Bavestrello [c], William T.M. Silva [d]

[a] Department of Production Engineering, University of Santa Catarina State, Campus Universitário Prof. Avelino Marcante s/n, Bairro Bom Retiro, Joinville-SC, CEP 89223-100, Brazil
[b] Center for Aerospace Structures, Colorado University, United States
[c] Institute for Computational and Mathematical Engineering, Stanford University, United States
[d] Department of Civil Engineering, University of Brasília, Brazil

ARTICLE INFO

Article history:
Received 8 May 2008
Received in revised form 11 October 2008
Accepted 17 October 2008
Available online 7 November 2008

Keywords:
Shell structures
Buckling and collapse
Co-rotational formulation
Layered plastic model
ANDES finite element

ABSTRACT

This study reveals an analysis of plastic buckling and collapse of thin shell structures. For this purpose, the co-rotational and layered plastic model as well as ANDES (Assumed Natural Deviatoric Strain) finite element formulations are used. The co-rotational kinematics formulation splits the translational and rotational deformations in a small deformation analysis. The ANDES finite element is modified to elasto-plastic ANDES finite element by the introduction of the von Mises yield criterion elastoplastic formulation on its original deformation model. In order to accommodate the plasticity formulation, the Gauss point layered integration is inserted through of thickness of the element to produce the internal force vector and material stiffness matrix. Special effort is devoted to maintain the consistency of the internal forces and tangent stiffness as well as to enhance the robustness of element level computations. The arc-length method is used to follow the postbuckling equilibrium path. Results are presented for several benchmark elastoplastic shell problems available in the present literature, which are generally in agreement with the present work.

1. Introduction

The non-linear analysis of shell structures is being investigated by researchers worldwide because of its large applicability in several areas of structural engineering, such as bridges, ships, airplanes, vehicles, roofing of large buildings, off-shore structures, etc. In such cases the structure may reach a deformed configuration after loading which differs significantly from that observed before loading. This happens basically because these structures have high self-resistance and are submitted to low body forces. The co-rotational kinematics formulation [1–12], which extracts deformational displacements from total ones, simulates large displacements with great accuracy and allows one to follow the equilibrium path in a geometrically non-linear analysis. However, when the internal stress state of the structure exceeds its maximum elastic limit stress, the plastic strain starts and the physically non-linear analysis becomes necessary [13–16] in order to simulate the structural behavior closest to reality. Two main approaches have been used in the literature to account for the material non-linearity due to plasticity in shell/plate formulation: the stress resultant approach (Ilyushin 1948, [17,18]) and the layer approach [19,20]. In the stress resultant approach, local plastic iterations are performed for each Gauss point on the middle surface over the area of the element. This case offers the advantage of less computational effort. On the other hand, its disadvantage is that its yield function has corners which makes the direct use of standard material coefficients impossible. In the layer approach, local plastic iterations are performed for each Gauss point along thickness and over the area of the element. This case reveals the following advantages: direct use of the local plasticity model and material coefficients because its yield function does not have corners; well-documented local plastic integration algorithm; a more precise distribution of plasticity through of thickness. As regards disadvantages, the layer approach presents greater computational effort and a specific treatment for plane stress needs to be implemented. The stress resultant approach has been used in the literature with Total Lagrangian, Updated Lagrangian [21], and co-rotational [18] kinematics descriptions. The layer approach has been used in the literature with Total Lagrangian and Updated Lagrangian kinematics descriptions. The layer plasticity approach has been developed in this work with the co-rotational description. The three-node triangular shell finite element based on the ANDES formulation is used to model shell structures. The linear version of this element was developed by Felippa and Militello in 1992 [22]. Some changes have been introduced to the basic concepts of the ANDES formulation in order to accommodate the physically non-linear analysis. In order to make the calculus of the internal force vector and of the

* Corresponding author. Tel.: +55 47 4009 7830; fax: +55 47 4009 7940.
E-mail address: nelviodc@yahoo.com.br (N.D. Cortivo).

0045-7825/$ - see front matter © 2008 Elsevier B.V. All rights reserved.
doi:10.1016/j.cma.2008.10.013

stiffness tangent matrix more general as well as to maintain their consistency and to enhance the robustness of the element level computations, the tangent stiffness is derived directly from the internal force vector. This procedure results in a new term for the tangent stiffness of the ANDES element introduced by this work: the coupling term between basic and high-order stiffness. The new methodology is set with the Consistent Symmetrizable Self-Equilibrated co-rotational formulation (CSSE) developed by Haugen [10] in his thesis. The main proposal of this work is to perform both geometrically and physically non-linear analysis for thin shell structures, applying respectively and together the CSSE co-rotational formulation and the layer approach plastic model, via the modified ANDES finite element and Simo's plasticity formulation.

2. Kinematics of the shell element

The kinematics used herein is the co-rotational formulation, which has been described in details in many papers, e.g. by Felippa and Haugen [11] and Battini [12]. This formulation extracts the deformational displacements from the total ones (Fig. 1), to simulate large displacements in small strain domain. Hence, its is necessary to establish the deformational displacements $\boldsymbol{v}_d^e$ vector in local frame, which stores the translational and rotational degrees of freedom for each node of the element:

$$(\boldsymbol{v}_d^e)^T = [(\boldsymbol{u}_{d1}^e)^T, (\boldsymbol{\theta}_{d1}^e)^T, \ldots, (\boldsymbol{u}_{dN}^e)^T, (\boldsymbol{\theta}_{dN}^e)^T]. \tag{1}$$

In Eq. (1), $\boldsymbol{u}_{dN}^e$ and $\boldsymbol{\theta}_{d1}^e$ are the translational and rotational degrees of freedom of the node N. The vector $\boldsymbol{v}_d^e$ is used in Eq. (45).

2.1. Translation of a shell element node, from the initial C_0 to the current C_n configuration

If one considers a shell element node, which moves from the initial position given by the position vector $\boldsymbol{r}_0$ to the deformed position given by the position vector $\boldsymbol{r}_n$ (Fig. 1), the nodal displacements vector is

$$\boldsymbol{u} = \boldsymbol{u}_R + \boldsymbol{u}_d. \tag{2}$$

In Eq. (2), the rigid body displacements $\boldsymbol{u}_R$ take place from initial C_0 to co-rotated C_R configuration. The deformational displacements $\boldsymbol{u}_d$ take place from co-rotated C_R to current C_n configuration. The vector $\boldsymbol{u}_d$ is obtained by algebraic manipulations of Eq. (2), taking into account geometrical considerations concerned to initial, co-rotated and current configurations. This vector has to be taken to local frame $\boldsymbol{u}_d^e$, in order to be ready for application in Eq. (1).

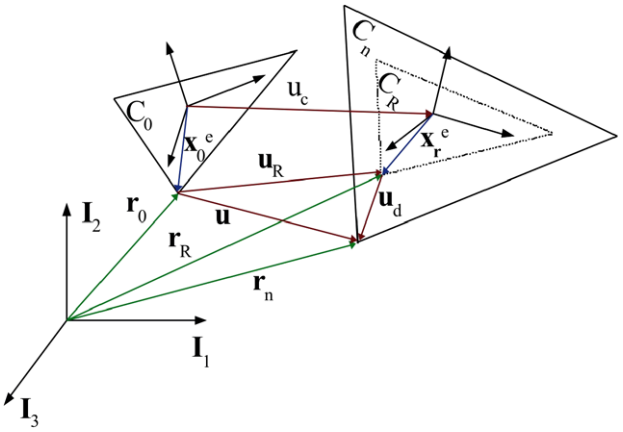

Fig. 1. Nodal translation of the shell element.

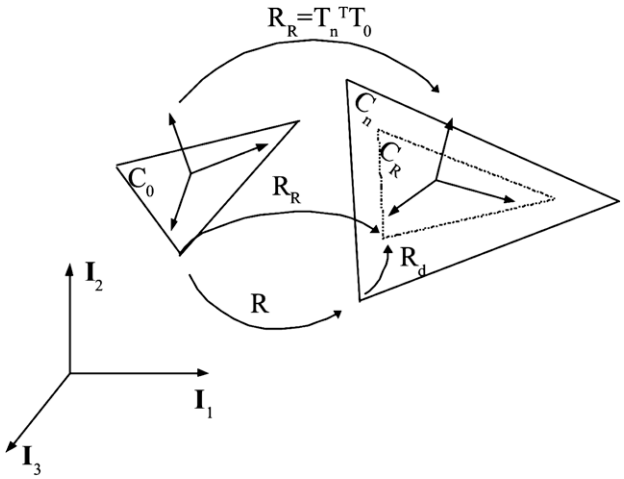

Fig. 2. Nodal rotation of the shell element.

2.2. Rotation of a shell element node, from the initial C_0 to the current C_n configuration

The rotation of a shell element node may be represented by a rotation tensor $\boldsymbol{R}$, from the initial C_0 to the final C_n configuration (Fig. 2). One may assume that tensor $\boldsymbol{R}$ is the decomposition of the rigid body $\boldsymbol{R}_R$ and deformational $\boldsymbol{R}_d$ rotation, as follows:

$$\boldsymbol{R} = \boldsymbol{R}_d \boldsymbol{R}_R. \tag{3}$$

The deformational rotation in global frame may be extracted as follows:

$$\boldsymbol{R}_d = \boldsymbol{R}\boldsymbol{R}_R^T = \boldsymbol{R}\boldsymbol{T}_0^T\boldsymbol{T}_n. \tag{4}$$

This deformational rotation may be expressed in local frame:

$$\boldsymbol{R}_d^e = \boldsymbol{T}_n\boldsymbol{R}_d\boldsymbol{T}_n^T = \boldsymbol{T}_n\boldsymbol{R}\boldsymbol{T}_0^T, \tag{5}$$

which is assumed small but finite. In Eqs. (4) and (5), $\boldsymbol{T}$ is a linear transformation matrix and $\boldsymbol{T}^T$ is its transposed matrix.

The rotations in 3D space are not commutative like they are in 2D space. Hence, it becomes necessary (see [23–25,19]) either to obtain the rotation tensor $\boldsymbol{R}$ or to extract the rotation pseudo-vector $\boldsymbol{\theta}$ from a given rotation tensor, for each node of the element. This pseudo-vector, since it comes from Eq. (5), may be identified as deformational rotational degrees of freedom $\boldsymbol{\theta}_d^e$ in local frame, which is ready to be used in Eq. (1).

3. Elastoplasticity formulation

Two main approaches have been used in the literature to account the material non-linearity due plasticity, in shell/plate formulation, which are: stress resultant approach (Ilyushin 1948) and layer approach (originally mainly used with the so called *degenerated* approach of shell modeling). In the stress resultant case (plastic model directly written in term of shell quantities), the local plastic iterations are performed for each gauss point on the middle surface over the area of the element. In this case the goal is to output the stress resultant and the tangent operator from the plastic iteration, in order to calculate the force vector and the tangent stiffness matrix by the integration over the area of the element. In the layer approach case, the local plastic iterations are performed for each gauss point along thickness and over the area of the element. This means that each gauss point along thickness of the element corresponds to a layer. In this case, the goal is output the stress and the tangent modulus from the plastic iteration, in order to calculate the stress resultant and the tangent operator

(shell quantities) by the integration along thickness of the element, and subsequently to calculate the force vector and the tangent stiffness matrix by the integration over the area of the element.

The stress resultant approach have been used in the literature with Total Lagrangian (TL), Updated Lagrangian (UL) [21] and co-rotational (CR) [18] kinematics descriptions. The layer approach have been done in the literature with Total Lagrangian (TL) and Updated Lagrangian (UL) kinematics descriptions. *The layer approach with co-rotational (CR) description has been developed in this work.*

The resultant approach has as advantage less computational effort. But as disadvantages, in this case the yield function has corners and one can not uses directly the material parameters obtained from material testing. The layer approach has as advantages: no corners in the yield functions; directly use of the local plasticity model and material coefficients; local plastic integration algorithm well documented; and more precise distribution of the plasticity through of thickness (more precise limit load, buckling and bifurcation prediction). As disadvantages, the layer approach presents more computational effort and specific treatment for plane stresses has to be figured out.

There exist in the literature various ways to use the elastoplasticity formulation to analyze the behaviour of a structure under applied loading. Both are based on the concept of Closest Point Projector Method (CPPM) [14,26,15,27,13]. In this work the Simo's/CPPM [13] elastoplasticity formulation/algorithm has been used. For simplicity, but without any loss of generality, the yield criterion and the hardening rule of interest in this work are Von Mises criterium, perfectly plastic material and isotropic hardening rule. For the isotropic hardening rule, the linear isotropic hardening and the exponential isotropic hardening are considered. The analysis is rate independent, and the associated flow rule, which allows the analysis without corners in the yield functions, is considered. Then, a short description of the Simo's/CPPM formulation/algorithm is shown in this subsection.

3.1. Elastoplasticity formulation for the isotropic hardening rule – Simo/CPPM elastoplasticity formulation

Simo [13] introduced in the classic elastoplasticity formulation [14,26,15,27,13] a "scaled" plastic multiplier $\dot{\gamma}$, which has the following relation to the classic plastic multiplier $\dot{\lambda}$:

$$\dot{\gamma} = \kappa \frac{\dot{\lambda}}{\|\boldsymbol{s}\|}. \tag{6}$$

Then, the classic elastoplasticity formulation can be re-written as follows:

$$\boldsymbol{\sigma} = \boldsymbol{C}_e(\varepsilon - \varepsilon_p), \tag{7}$$
$$\dot{\varepsilon}_p = \dot{\gamma}\boldsymbol{P}\boldsymbol{\sigma}, \tag{8}$$
$$\dot{p} = \frac{\dot{\gamma}}{\kappa}\|\boldsymbol{s}\| = \frac{\dot{\gamma}}{\kappa}\sqrt{\kappa\boldsymbol{\sigma}^T\boldsymbol{P}\boldsymbol{\sigma}}, \tag{9}$$
$$f(\boldsymbol{\sigma}, R) \equiv \|\boldsymbol{s}\| - R(p) = 0, \tag{10}$$

where $\boldsymbol{\sigma}$ is the current state stresses; $\boldsymbol{C}_e$ is the elastic tangent matrix; ε is the total strain in the current step; ε_p is the cumulative plastic strain at the previous step; $\dot{\lambda}$ is the plastic multiplier; p is the effective plastic strain; $\boldsymbol{s} \equiv \overline{\boldsymbol{P}}\boldsymbol{\sigma}$ is the deviatoric part of the stress state; $\|\boldsymbol{s}\|$ is the norm of the deviatoric part of the stress state; and $R(p)$ represents the isotropic hardening rule. Eq. (7) is the elastic equation, which allows one to calculate the stress state in whatever point on the path equilibrium; Eqs. (8) and (9) represent the flow rule of the plastic model; and Eq. (10) is the yield function.

In Eq. (10), $R(p)$ can be chosen like below:

- perfectly plastic material: $R(p) = \sigma_0$
- linear isotropic hardening material: $R(p) = \sigma_0 + Kp$
- exponential isotropic hardening material: $R(p) = \sigma_0 + Q(1 - e^{-bp})$

where K, Q and b are constant material parameters.

Usually, Eqs. (7)–(10) can be time discretized using the (implicit) Euler backward scheme, as follows: knowing all data from end of the previous step, (i.e. $\boldsymbol{\sigma}_n$, ε_{p_n}, p_n, ...), the problem is then to find $\boldsymbol{\sigma}_{n+1}$, $\varepsilon_{p_{n+1}}$, p_{n+1} solutions for the current step:

$$\boldsymbol{\sigma}_{n+1} = \boldsymbol{\sigma}^\star - \boldsymbol{C}_e\Delta\varepsilon_{p_{n+1}} = \boldsymbol{\sigma}^\star - \Delta\gamma\boldsymbol{C}_e\boldsymbol{P}\boldsymbol{\sigma}_{n+1}, \tag{11}$$
$$\Delta\varepsilon_{p_{n+1}} = \Delta\gamma\boldsymbol{P}\boldsymbol{\sigma}_{n+1}, \tag{12}$$
$$\Delta p = \frac{\Delta\gamma}{\kappa}\sqrt{\kappa\boldsymbol{\sigma}_{n+1}^T\boldsymbol{P}\boldsymbol{\sigma}_{n+1}}, \tag{13}$$
$$f(\boldsymbol{\sigma}_{n+1}, R_{n+1}) \equiv \|\boldsymbol{s}_{n+1}\| - R(p_{n+1}) = 0, \tag{14}$$

where by definition: $\Delta\square$ or $\Delta\square_{n+1} \equiv \square_{n+1} - \square_n$; $\boldsymbol{s}_{n+1} \equiv \overline{\boldsymbol{P}}\boldsymbol{\sigma}_{n+1}$ is the deviatoric part of the current stress state; and $\boldsymbol{\sigma}^\star$ is the *trial* stress, i.e. the value of $\boldsymbol{\sigma}_{n+1}$ assuming the step is elastic.

When performing plastic iterations (Euler backward scheme), one has to consider the following relations, which are the Kuhn–Tucker conditions:

$$\Delta\lambda \geqslant 0, \quad f \leqslant 0, \quad \Delta\lambda f = 0. \tag{15}$$

The Kuhn–Tucker conditions establishes that the plastic strain never decreases and that the stress state has to be on the yield surface, for the rate independent analysis.

In order to calculate the deviatoric part of the current stresses state (in a plane stress consideration) and the direction of the plastic flow, one can assume, also by definition:

$$\overline{\boldsymbol{P}} : \mathbb{S}_P \mapsto \mathbb{S}_D, \quad \boldsymbol{s} \equiv \overline{\boldsymbol{P}}\boldsymbol{\sigma}, \quad \overline{\boldsymbol{P}} \equiv \frac{1}{3}\begin{bmatrix} 2 & -1 & 0 \\ -1 & 2 & 0 \\ 0 & 0 & 3 \end{bmatrix}, \tag{16}$$

where $\mathbb{S}_P$ is the space of the plane stress tensor and $\mathbb{S}_D$ is the space of the deviatoric plane stress tensor, and

$$\|\boldsymbol{s}\|^2 \equiv \kappa\boldsymbol{s}^T\boldsymbol{A}\boldsymbol{s}, \quad \boldsymbol{s} \in \mathbb{S}_D, \quad \boldsymbol{A} \equiv \begin{bmatrix} 2 & 1 & 0 \\ 1 & 2 & 0 \\ 0 & 0 & 2 \end{bmatrix}, \tag{17}$$

where *kappa* is just a scale factor (which is 2/3 for the Von Mises criterion).

By the assumption that the step is elastic, the *trial* stress can be written as

$$\boldsymbol{\sigma}^\star \equiv \boldsymbol{C}_e(\varepsilon_{n+1} - \varepsilon_{p_n}) = \boldsymbol{\sigma}_n + \boldsymbol{C}_e\Delta\varepsilon_{n+1}, \tag{18}$$

where $\Delta\varepsilon_{n+1} \equiv \varepsilon_{n+1} - \varepsilon_n$.

In a displacement finite element formulation, $\Delta\varepsilon_{n+1}$ is usually a *given* input parameter of the (local) plastic algorithm (i.e. deduced from the displacement increment of the outer structural equilibrium loop). The local plastic algorithm is then usually called a *strain-driven* scheme.

Remark. From now on, for simplicity every $\boldsymbol{\sigma}_{n+1}$ is going to be replaced by $\boldsymbol{\sigma}$.

3.2. Algorithm for the Simo/CPPM elastoplasticity formulation

In order to evaluate Eqs. (11)–(13), first one needs to calculate $\Delta\gamma$, which can be determined by solving the scalar yield function equation below and applying the Newton iteration method:

$$f(\boldsymbol{\sigma}(\Delta\gamma), R(p_{n+1}(\Delta\gamma))) = 0. \tag{19}$$

In Eq. (19), $\boldsymbol{\sigma}(\Delta\gamma)$ is given by

$$[\boldsymbol{C}_e^{-1} + \Delta\gamma\boldsymbol{P}]\boldsymbol{\sigma} = \boldsymbol{C}_e^{-1}\boldsymbol{\sigma}^\star \Rightarrow \boldsymbol{\sigma} = \boldsymbol{\Xi}(\Delta\gamma)\boldsymbol{C}_e^{-1}\boldsymbol{\sigma}^\star, \tag{20}$$

where

$$\Xi(\Delta\gamma) \equiv [\boldsymbol{C}_e^{-1} + \Delta\gamma \boldsymbol{P}]^{-1}.$$

The evaluation of $R(p_{n+1}(\Delta\gamma))$ and $\frac{dR}{d\gamma} = \frac{\partial R}{\partial p}\frac{dp}{d\gamma}$ is also necessary, which is required in the Newton loop. Then, considering Eq. (6):

$$p_{n+1}(\Delta\gamma) = p_n + \Delta p = p_n + \frac{\Delta\gamma}{\kappa}\|\boldsymbol{s}_{n+1}\| \tag{21}$$

and

$$dp = \frac{1}{\kappa}(d\gamma\|\boldsymbol{s}_{n+1}\| + \Delta\gamma d\|\boldsymbol{s}_{n+1}\|) = \frac{1}{\kappa}(\|\boldsymbol{s}_{n+1}\|d\gamma + \Delta\gamma \boldsymbol{N}_{n+1}^T d\boldsymbol{\sigma}), \tag{22}$$

where $\boldsymbol{N} \equiv \kappa\frac{\boldsymbol{s}}{\|\boldsymbol{s}\|}$ and $\boldsymbol{N}_{n+1} \equiv \kappa\frac{\boldsymbol{s}_{n+1}}{\|\boldsymbol{s}_{n+1}\|}$ (by definition) give the direction of the plastic flow, and $d\boldsymbol{\sigma}_{n+1}$ is obtained by deriving Eq. (11), as follows:

$$d\boldsymbol{\sigma} = -\Xi(\Delta\gamma)\boldsymbol{P}\boldsymbol{\sigma}d\gamma. \tag{23}$$

Finally, dp can be expressed as

$$dp = \frac{1}{\|\boldsymbol{s}\|}\left[\frac{\|\boldsymbol{s}\|^2}{\kappa} - \Delta\gamma\boldsymbol{\sigma}^T\boldsymbol{P}\Xi\boldsymbol{P}\boldsymbol{\sigma}\right]d\gamma. \tag{24}$$

For the application of the Newton iteration method, one may consider the consistency condition $f + df = 0$, that is the linearization of f around of the current $\Delta\gamma$, as follows:

$$f + df = f + \left(\frac{\partial\|\boldsymbol{s}\|}{\partial\boldsymbol{\sigma}}\frac{d\boldsymbol{\sigma}}{d\gamma} - \frac{dR}{d\gamma}\right)\delta\gamma = f + \left(\boldsymbol{N}^T\frac{d\boldsymbol{\sigma}}{d\gamma} - \frac{dR}{d\gamma}\right)\delta\gamma = 0. \tag{25}$$

The Newton iteration on Eq. (19) provides the following iterative update of $\Delta\gamma$:

$$\Delta\gamma \leftarrow \Delta\gamma + \delta\gamma, \quad \delta\gamma = \frac{\|\boldsymbol{s}\|f_{n+1}}{\frac{dR}{dp}\frac{\|\boldsymbol{s}\|^2}{\kappa} + \theta_2\boldsymbol{\sigma}^T\boldsymbol{P}\Xi\boldsymbol{P}\boldsymbol{\sigma}}, \tag{26}$$

where $\theta_2 \equiv \kappa - \frac{dR}{dp}\Delta\gamma$.

Remark. Eq. (19) can be solved in a general way by Newton iteration, or by closed solution for simple isotropic hardening models (i.e. isotropic elasticity with linear isotropic hardening model using "$\tilde{f}$" as yield function $\mapsto$ quartic equation in $\Delta\bar{\gamma} \equiv E\Delta\gamma$).

Note that one can also "square" the yield function:

$$f(\boldsymbol{\sigma}, R) = 0 \Longleftrightarrow \tilde{f} \equiv f(\boldsymbol{\sigma}, R) \times (\|\boldsymbol{s}\| + R(p)) = \|\boldsymbol{s}\|^2 - R^2(p) = 0 \tag{27}$$

and determine $\Delta\gamma$ by solving

$$\tilde{f}(\boldsymbol{\sigma}(\Delta\gamma), R(\Delta\gamma)) = 0. \tag{28}$$

Consistent elastoplastic tangent modulus.

In order to express Eqs. (23) and (24) by the relation between $d\gamma$ and $d\boldsymbol{\varepsilon}$, one can write

$$d\boldsymbol{\sigma} = \Xi(\Delta\gamma)[d\boldsymbol{\varepsilon} - \boldsymbol{P}\boldsymbol{\sigma}d\gamma] \tag{29}$$

and

$$dp = \frac{\|\boldsymbol{s}\|}{\kappa}d\gamma + \frac{\Delta\gamma}{\kappa}\boldsymbol{N}^T d\boldsymbol{\sigma} = \left[\frac{\|\boldsymbol{s}\|}{\kappa} - \frac{\Delta\gamma}{\kappa}\boldsymbol{N}^T\Xi\boldsymbol{P}\boldsymbol{\sigma}\right]d\gamma + \frac{\Delta\gamma}{\kappa}\boldsymbol{N}^T\Xi d\boldsymbol{\varepsilon}. \tag{30}$$

Again coming from the consistency condition, in which $df = 0$, and in order to obtain the consistent tangent modulus, one can express the following relations:

$$df = \boldsymbol{N}^T d\boldsymbol{\sigma} - \frac{dR}{dp}dp = 0 \Rightarrow \left[\frac{dR}{dp}\frac{\|\boldsymbol{s}\|}{\kappa} + \frac{\theta_2}{\kappa}\boldsymbol{N}^T\Xi\boldsymbol{P}\boldsymbol{\sigma}\right]d\gamma = \frac{\theta_2}{\kappa}\boldsymbol{N}^T\Xi d\boldsymbol{\varepsilon}. \tag{31}$$

As $\boldsymbol{N} \equiv \kappa\frac{\boldsymbol{P}\boldsymbol{\sigma}}{\|\boldsymbol{s}\|}$, and introducing β as: $\beta \equiv \frac{1}{\kappa}\frac{\|\boldsymbol{s}\|^2}{\theta_2}\frac{\frac{dR}{dp}}{\boldsymbol{\sigma}^T\boldsymbol{P}\Xi\boldsymbol{P}\boldsymbol{\sigma}}$, $d\gamma$ can be written as

$$d\gamma = \frac{\theta_2\boldsymbol{\sigma}^T\boldsymbol{P}\Xi d\boldsymbol{\varepsilon}}{\frac{dR}{dp}\frac{\|\boldsymbol{s}\|^2}{\kappa} + \theta_2\boldsymbol{\sigma}^T\boldsymbol{P}\Xi\boldsymbol{P}\boldsymbol{\sigma}} = \frac{1}{(1+\beta)}\frac{\boldsymbol{\sigma}^T\boldsymbol{P}\Xi d\boldsymbol{\varepsilon}}{\boldsymbol{\sigma}^T\boldsymbol{P}\Xi\boldsymbol{P}\boldsymbol{\sigma}}, \tag{32}$$

so that

$$d\boldsymbol{\sigma} = \left[\Xi - \frac{1}{(1+\beta)}\frac{(\Xi\boldsymbol{P}\boldsymbol{\sigma})(\Xi\boldsymbol{P}\boldsymbol{\sigma})^T}{\boldsymbol{\sigma}^T\boldsymbol{P}\Xi\boldsymbol{P}\boldsymbol{\sigma}}\right]d\boldsymbol{\varepsilon} = \left[\Xi - \frac{NN^T}{1+\beta}\right]d\boldsymbol{\varepsilon}, \tag{33}$$

where

$$N \equiv \frac{\Xi\boldsymbol{P}\boldsymbol{\sigma}}{\sqrt{\boldsymbol{\sigma}^T\boldsymbol{P}\Xi\boldsymbol{P}\boldsymbol{\sigma}}}.$$

Thus, the consistent tangent elastoplastic modulus is

$$\boldsymbol{C}_T = \Xi - \frac{NN^T}{1+\beta}. \tag{34}$$

Remark. The Simo's procedure can be greatly simplified in the isotropic case, because $\boldsymbol{C}_e$ and $\boldsymbol{P}$ are diagonalisable in the same basis

$$\boldsymbol{P} = \boldsymbol{Q}\cdot\boldsymbol{\Lambda}_P\cdot\boldsymbol{Q}^T, \quad \boldsymbol{C}_e = \boldsymbol{Q}\cdot\boldsymbol{\Lambda}_C\cdot\boldsymbol{Q}^T \text{ with } \boldsymbol{Q}^{-1} = \boldsymbol{Q}^T$$

$$\boldsymbol{Q} \equiv \frac{1}{\sqrt{2}}\begin{bmatrix}1 & 1 & 0\\ -1 & 1 & 0\\ 0 & 0 & \sqrt{2}\end{bmatrix}, \quad \boldsymbol{\Lambda}_P \equiv \begin{bmatrix}\frac{1}{3} & 0 & 0\\ 0 & 1 & 0\\ 0 & 0 & 2\end{bmatrix}, \quad \boldsymbol{\Lambda}_C \equiv \begin{bmatrix}\frac{E}{1-\nu} & 0 & 0\\ 0 & 2\mu & 0\\ 0 & 0 & \mu\end{bmatrix},$$

so that

$$\Xi(\Delta\gamma) = \boldsymbol{Q}[\boldsymbol{\Lambda}_C^{-1} + \Delta\gamma\boldsymbol{\Lambda}_P]^{-1}\boldsymbol{Q}^T = \boldsymbol{Q}\bar{\Xi}\boldsymbol{Q}^T \tag{35}$$

and

$$\boldsymbol{\sigma}_{n+1} = \boldsymbol{Q}\bar{\Xi}\boldsymbol{\Lambda}_C^{-1}\boldsymbol{Q}^T\boldsymbol{\sigma}^\star \Rightarrow \boldsymbol{Q}^T\boldsymbol{\sigma}_{n+1} = \bar{\Xi}\boldsymbol{\Lambda}_C^{-1}\boldsymbol{Q}^T\boldsymbol{\sigma}^\star = \boldsymbol{\Gamma}(\Delta\gamma)\boldsymbol{Q}^T\boldsymbol{\sigma}^\star \tag{36}$$

with

$$\boldsymbol{\Gamma}(\Delta\gamma) \equiv [\boldsymbol{I} + \Delta\gamma\boldsymbol{\Lambda}_P\boldsymbol{\Lambda}_C]^{-1} = \begin{bmatrix}\frac{1}{1+\frac{E}{3(1-\nu)}\Delta\gamma} & 0 & 0\\ 0 & \frac{1}{1+2\mu\Delta\gamma} & 0\\ 0 & 0 & \frac{1}{1+2\mu\Delta\gamma}\end{bmatrix}. \tag{37}$$

We can then directly work with the new variable $\boldsymbol{\xi} \equiv \boldsymbol{Q}^T\boldsymbol{\sigma}$:

$$\boldsymbol{\xi}_{n+1} = \boldsymbol{\Gamma}(\Delta\gamma)\boldsymbol{\xi}^\star, \tag{38}$$

$$\Delta p = \frac{\Delta\gamma}{\kappa}\sqrt{\kappa\boldsymbol{\xi}_{n+1}^T\boldsymbol{\Lambda}_P\boldsymbol{\xi}_{n+1}}, \tag{39}$$

$$f(\boldsymbol{\sigma}_{n+1}, R_{n+1}) \equiv \sqrt{\kappa\boldsymbol{\xi}_{n+1}^T\boldsymbol{\Lambda}_P\boldsymbol{\xi}_{n+1}} - R(p_{n+1}) = 0, \tag{40}$$

$$dp = \frac{1}{\kappa}\left(d\gamma\sqrt{\kappa\boldsymbol{\xi}^T\boldsymbol{\Lambda}_P\boldsymbol{\xi}} + \Delta\gamma d\left(\sqrt{\kappa\boldsymbol{\xi}^T\boldsymbol{\Lambda}_P\boldsymbol{\xi}}\right)\right), \tag{41}$$

$$\boldsymbol{\sigma}^T\boldsymbol{P}\Xi\boldsymbol{P}\boldsymbol{\sigma} = \boldsymbol{\xi}^T\boldsymbol{\Lambda}_P\bar{\Xi}\boldsymbol{\Lambda}_P\boldsymbol{\xi}, \quad \bar{\Xi} \equiv \begin{bmatrix}\frac{3E}{3(1-\nu)+E\Delta\gamma} & 0 & 0\\ 0 & \frac{2\mu}{1+2\mu\Delta\gamma} & 0\\ 0 & 0 & \frac{\mu}{1+2\mu\Delta\gamma}\end{bmatrix}. \tag{42}$$

4. Internal force vector and tangent stiffness matrix

In this chapter, it is initially explained how to obtain the internal force vector and the tangent stiffness matrix, in accordance with the CSSE formulation, for the ANDES finite element. The CSSE co-rotational formulation was proposed by Haugen in 1994 [10] and the ANDES finite element was first presented by Felippa and Militello in 1991/1992 [22,28]. Afterward the methodology proposed by this work is presented. This work uses the basic concepts of the CSSE and ANDES formulations, but it introduces some changes in the ANDES formulation, in order to develop the physi-

cally non-linear analysis and to improve the convergence of the elastoplastic algorithm, by developing the internal force vector and the stiffness tangent matrix in a general form.

4.1. Internal force vector and stiffness tangent matrix (CSSE formulation [10,18])

After a brief description of equations that govern the geometrical non-linear analysis, the internal force vector $\boldsymbol{F}$ and the stiffness tangent matrix $\boldsymbol{K}$ are developed in this section, following the CSSE co-rotational formulation. As Haugen has shown, this formulation allows a good performance for the element, when it concerns the self-equilibrium of the internal force vector, to the consistency and symmetrization of the stiffness tangent matrix and to the invariance and independence of the element.

4.1.1. Equations which govern the geometrically non-linear analysis

The global equilibrium equations of the geometrically non-linear analysis can be established, through of finite element method, by the residual force vector $\boldsymbol{R}$, which tends to disappear along a equilibrium path, as below:

$$\boldsymbol{R}(\boldsymbol{v},\lambda) = \boldsymbol{F}(\boldsymbol{v}) - \boldsymbol{P}(\lambda) = 0, \tag{43}$$

where $\boldsymbol{v} = \boldsymbol{v}(\lambda)$.

The vector $\boldsymbol{v}$ collects the global nodal degree of freedom (translational and rotational) of the structure; $\boldsymbol{F}$ is the internal force vector generated by the displacements $\boldsymbol{v}$; and $\boldsymbol{P}$ is the external load vector, which exists as a function of the load parameter λ.

Whether the residual force is zero, the first derivation of the equilibrium Eq. (43) in relation to the load parameter λ is also zero:

$$\frac{d\boldsymbol{R}}{d\lambda} = \frac{\partial \boldsymbol{F}}{\partial \boldsymbol{v}}\frac{d\boldsymbol{v}}{d\lambda} - \frac{d\boldsymbol{P}}{d\lambda} = \boldsymbol{K}\boldsymbol{w} - \boldsymbol{q} = \boldsymbol{0}. \tag{44}$$

In Eq. (44), $\boldsymbol{K}$ is the stiffness tangent matrix, $\boldsymbol{w}$ is the displacement incremental vector, and $\boldsymbol{q}$ is the load incremental vector.

4.1.2. Internal force vector (CSSE formulation [10,18])

In the CSSE formulation, the strain–displacement relation for the co-rotated C_R and current C_n configurations, in local frame ($\square^e$) is

$$\boldsymbol{\varepsilon}^e = \boldsymbol{B}^e \boldsymbol{v}_d^e, \tag{45}$$

where $\boldsymbol{v}_d^e$ is the vector of the deformational displacements, which exists between the co-rotated C_R and current C_n configurations; $\mathbf{B}^e$ is the curvature (bending) matrix or the extensional (membrane) matrix; and $\boldsymbol{\varepsilon}^e$ is the strain vector of the element. The linear elastic constitutive relation for this formulation, also in the local frame, is

$$\boldsymbol{\sigma}^e = \boldsymbol{C}^e \boldsymbol{\varepsilon}^e, \tag{46}$$

where C^e is the linear elastic material constitutive matrix and $\boldsymbol{\sigma}^e$ is the stress vector of the element.

If one considers the strain energy equation

$$\Phi = \frac{1}{2}\int_V (\boldsymbol{\varepsilon}^e)^T \boldsymbol{\sigma}^e dV, \tag{47}$$

and takes into account the minimal work Castigliano's theorem (and also considering Eqs. (45) and (46)), the internal force vector can be written in relation to the global frame as below:

$$\boldsymbol{F}(\boldsymbol{v}) = \boldsymbol{T}^T \boldsymbol{P}^{Te} \boldsymbol{H}^{Te} \int_V \boldsymbol{B}^{Te} \boldsymbol{C}^e \boldsymbol{B}^e dV \boldsymbol{v}_d^e, \tag{48}$$

where

$$\int_V \boldsymbol{B}^{Te} \boldsymbol{C}^e \boldsymbol{B}^e dV = \boldsymbol{K}_{LE}^e \tag{49}$$

is the material linear elastic tangent stiffness matrix of the element; $\boldsymbol{T}^T$ is the linear transformation matrix, which transforms the internal forces from local to global frame; $\boldsymbol{P}$ is the projection operator, which ensure the equilibrium of the internal force vector; and $\boldsymbol{H}$ is the projection operator, which acts on the rotate degrees of freedom of the element, in order to ensure the symmetry of the consistent tangent stiffness matrix. The consistent tangent stiffness matrix is derived from the internal force vector. See [18] for details about the matrices $\boldsymbol{P}$ and $\boldsymbol{H}$.

4.1.3. The consistent tangent stiffness matrix (CSSE formulation [10,18])

The tangent stiffness matrix is considered consistent since it is the variation of the internal forces $\boldsymbol{F}$, in relation to the displacements vector $\boldsymbol{v}$:

$$\delta \boldsymbol{F} = \frac{\partial \boldsymbol{F}}{\partial v_i}\delta v_i = \frac{\partial \boldsymbol{F}}{\partial \boldsymbol{v}}\delta \boldsymbol{v} = \boldsymbol{K}\delta \boldsymbol{v} \tag{50}$$

Taking into account Eqs. (48)–(50), one has

$$\begin{aligned}\delta \boldsymbol{F} = {} & \delta \boldsymbol{T}^T \boldsymbol{P}^{Te} \boldsymbol{H}^{Te} \boldsymbol{F}^e + \boldsymbol{T}^T \delta \boldsymbol{P}^{Te} \boldsymbol{H}^{Te} \boldsymbol{F}^e + \boldsymbol{T}^T \boldsymbol{P}^{Te} \delta \boldsymbol{H}^{Te} \boldsymbol{F}^e \\ & + \boldsymbol{T}^T \boldsymbol{P}^{Te} \boldsymbol{H}^{Te} \delta \boldsymbol{F}^e\end{aligned} \tag{51}$$

which also can be written as follows:

$$\delta \boldsymbol{F} = (\boldsymbol{K}_{GR} + \boldsymbol{K}_{GP} + \boldsymbol{K}_{GM} + \boldsymbol{K}_M)\delta \boldsymbol{v}. \tag{52}$$

Thus, for the co-rotational formulation CSSE, the consistent tangent stiffness matrix is

$$\boldsymbol{K} = \boldsymbol{K}_{GR} + \boldsymbol{K}_{GP} + \boldsymbol{K}_{GM} + \boldsymbol{K}_M, \tag{53}$$

where $\boldsymbol{K}_{GR}$ is the rotational geometric stiffness; $\boldsymbol{K}_{GP}$ is the equilibrium projection geometric stiffness; $\boldsymbol{K}_{GM}$ is the moment correction geometric stiffness; and $\boldsymbol{K}_M$ is the material stiffness of the element, which after algebraic manipulations becomes as below:

$$\boldsymbol{K}_M = \boldsymbol{T}^T \boldsymbol{P}^{Te} \boldsymbol{H}^{Te} \boldsymbol{K}_{LE}^e \boldsymbol{H}^e \boldsymbol{P}^e \boldsymbol{T}, \tag{54}$$

where $\boldsymbol{K}_{LE}^e$ is the material linear elastic tangent stiffness matrix of the element, as shown in (49). See [18] for details about the matrices $\boldsymbol{K}_{GR}$, $\boldsymbol{K}_{GP}$ and $\boldsymbol{K}_{GM}$.

4.1.4. Material linear elastic tangent stiffness matrix (ANDES Element)

The ANDES finite element was first developed by Felippa and Militello in 1991/1992 [22,28] and later by Felippa's works [29–34]. The ANDES formulation generates the material linear elastic tangent stiffness matrix $\boldsymbol{K}_{LE}^e$ and the internal force vector $\boldsymbol{F}$ of the element, both used in the CSSE formulation.

The ANDES element has six degrees of freedom each node (three membrane components and three bending components). Among the membrane components there exists the "drilling" degree of freedom. The tangent stiffness matrix of the ANDES element is split in two parts, which are basic and higher order stiffness. For the basic stiffness $\boldsymbol{K}_b$, the stress is assumed constant in the element. This approximation has been first used by Bergan and Hanssen [35] and later by Bergan and Nygard [4,9]. Thus, the basic stiffness matrix of the ANDES element is

$$\boldsymbol{K}_b = \frac{1}{V}\boldsymbol{L}\boldsymbol{C}\boldsymbol{L}^T. \tag{55}$$

In the above equation, V is the volume of the element, which is replaced by either A (area), if one has a shell element, or L (length), if one has a bar element; $\boldsymbol{C}$ is the linear elastic constitutive matrix; and $\boldsymbol{L}$ is the matrix which has the deformational field of the element, and also is responsible for the stress lumping in the nodes of the element.

The higher order stiffness $\boldsymbol{K}_h$ takes into account the assumed natural strain, instead of being based in the displacement modes.

For its construction, the deviatoric strains of the element are used, which are the subtraction of the principal strains from the total ones. In this way, the higher order tangent stiffness matrix of the ANDES element is

$$\boldsymbol{K}_h = \int_V \boldsymbol{B}_d^T \boldsymbol{C} \boldsymbol{B}_d dV, \tag{56}$$

where $\boldsymbol{B}_d$ is the matrix which represents the deviatoric curvatures (bending) or deviatoric extensions (membrane). Thus, the material linear elastic tangent stiffness matrix for the ANDES element is

$$\boldsymbol{K}_{LE}^e = \boldsymbol{K}_b + \boldsymbol{K}_h = \frac{1}{V}\boldsymbol{L}\boldsymbol{C}\boldsymbol{L}^T + \int_V \boldsymbol{B}_d^T \boldsymbol{C} \boldsymbol{B}_d dV. \tag{57}$$

Remark. From now on, the super-index $\square^e$, which represents the local frame, is going to be omitted. But every formulation about the force vector $\boldsymbol{F}$ and the material tangent matrix $\mathbf{K}_T$ is supposed to be in the local frame.

4.2. Elastoplastic ANDES element

Since the main proposal of this work is to perform geometrically and physically non-linearities analysis for thin shell structures, applying the layer approach (and using the CSSE co-rotational formulation, the ANDES thin shell element and Simo's plasticity formulation) as plastic model, in this section is presented a new way to obtain the internal force vector and the tangent stiffness matrix for the ANDES thin shell finite element. The basic concepts of the ANDES formulation are used herein, but this work introduces some changes in the ANDES formulation, in order to develop the physically non-linear analysis and to improve the convergence of the elastoplastic algorithm, by developing the internal force vector and the stiffness tangent matrix in a general form. *The new methodology is set with the CSSE co-rotational formulation.*

4.2.1. Internal force vector and tangent stiffness matrix

Following the ANDES framework, for a *given* elementary stress field $\boldsymbol{\sigma}$, one can split the elementary internal force vector $\boldsymbol{F}_{int}$ (in local frame) into *low or basic* ($\boldsymbol{F}_{int,B}$) and *higher* ($\boldsymbol{F}_{int,H}$) order contributions, as follows:

$$\boldsymbol{F}_{int} \equiv \boldsymbol{F}_{int,B} + \boldsymbol{F}_{int,H} = \boldsymbol{L}\bar{\boldsymbol{\sigma}} + \int_{\Omega_e} \boldsymbol{B}_d^T \boldsymbol{\sigma}_d d\Omega \tag{58}$$

where $\bar{\boldsymbol{\sigma}}$ is the *constant or basic* part and $\boldsymbol{\sigma}_d$ the "deviatoric" part of the stress field $\boldsymbol{\sigma}$, which can be defined as

$$\bar{\boldsymbol{\sigma}} \equiv \frac{1}{mes(\Omega_e)} \int_{\Omega_e} \boldsymbol{\sigma} d\Omega, \boldsymbol{\sigma}_d \equiv \boldsymbol{\sigma} - \bar{\boldsymbol{\sigma}} \tag{59}$$

where $mes(\Omega_e)$ is the "measure" of the domain Ω_e in the element (i.e. the volume if Ω_e is a 3D domain, the area if Ω_e is a 2D domain, or the length if Ω_e is a 1D domain). In the sequel, $mes(\Omega_e)$ will be abbreviated simply by Ω_e. $\boldsymbol{L}$ is the *constant* nodal force lumping operator, and $\boldsymbol{B}_d$ is the "*deviatoric*" part of the "high order" ANDES strain–displacement operator $\boldsymbol{B}$, defined as

$$\boldsymbol{B}_d \equiv \boldsymbol{B} - \bar{\boldsymbol{B}}, \text{ with } \bar{\boldsymbol{B}} \equiv \frac{1}{\Omega_e}\int_\Omega \boldsymbol{B} d\Omega. \tag{60}$$

By construction, $\boldsymbol{B}_d$ has the following useful property:

$$\int_{\Omega_e} \boldsymbol{B}_d d\Omega = 0. \tag{61}$$

Accordingly, the strain field $\boldsymbol{\varepsilon}$ can be split into basic and higher order contribution as

$$\boldsymbol{\varepsilon} = \bar{\boldsymbol{\varepsilon}} + \boldsymbol{\varepsilon}_d, \quad \bar{\boldsymbol{\varepsilon}} \equiv \frac{1}{\Omega_e}\int_\Omega \boldsymbol{\varepsilon} d\Omega = \frac{1}{\Omega_e}\boldsymbol{L}\boldsymbol{v}\boldsymbol{\varepsilon}_d = \boldsymbol{B}_d \boldsymbol{v}. \tag{62}$$

The (consistent tangent) stiffness matrix is obtained by deriving the internal force vector $\boldsymbol{F}_{int}$:

$$d\boldsymbol{F}_{int} = \boldsymbol{K}_T d\boldsymbol{u}, d\boldsymbol{F}_{int} = \boldsymbol{L} d\bar{\boldsymbol{\sigma}} + \int_{\Omega_e} \boldsymbol{B}_d^T d\boldsymbol{\sigma}_d d\Omega. \tag{63}$$

Splitting $d\boldsymbol{\varepsilon}$ as $d\bar{\boldsymbol{\varepsilon}} + d\boldsymbol{\varepsilon}_d$, we obtain (noting that $d\bar{\boldsymbol{\varepsilon}}$ is constant throughout Ω_e):

$$d\bar{\boldsymbol{\sigma}} \equiv \frac{1}{\Omega_e}\int_\Omega d\boldsymbol{\sigma} d\Omega = \frac{1}{\Omega_e}\int_\Omega \boldsymbol{C}_t d\boldsymbol{\varepsilon} d\Omega = \bar{\boldsymbol{C}}_t^e d\bar{\boldsymbol{\varepsilon}} + \frac{1}{\Omega_e}\int_\Omega \boldsymbol{C}_t d\boldsymbol{\varepsilon}_d d\Omega, \tag{64}$$

where $\bar{\boldsymbol{C}}_t$ is the constant part on Ω_e of the constitutive (consistent) tangent operator $\boldsymbol{C}_t$:

$$d\boldsymbol{\sigma} = \boldsymbol{C}_t d\boldsymbol{\varepsilon}, \quad \bar{\boldsymbol{C}}_t \equiv \frac{1}{\Omega_e}\int_{\Omega_e} \boldsymbol{C}_t d\Omega \tag{65}$$

and with $d\boldsymbol{\sigma}_d = d\boldsymbol{\sigma} - d\bar{\boldsymbol{\sigma}}$,

$$\int_{\Omega_e} \boldsymbol{B}_d^T d\boldsymbol{\sigma}_d d\Omega = \int_{\Omega_e} \boldsymbol{B}_d^T \boldsymbol{C}_t d\boldsymbol{\varepsilon}_d d\Omega + \int_{\Omega_e} \boldsymbol{B}_d^T (\boldsymbol{C}_t - \bar{\boldsymbol{C}}_t) d\bar{\boldsymbol{\varepsilon}} d\Omega + \frac{1}{\Omega_e}\int_{\Omega_e} \boldsymbol{B}_d^T \left(\int_{\Omega_e} \boldsymbol{C}_t d\boldsymbol{\varepsilon}_d d\Omega\right) d\Omega. \tag{66}$$

Using the property (61) of $\boldsymbol{B}_d$, the last term of (66) is *null*:

$$\frac{1}{\Omega_e}\int_{\Omega_e} \boldsymbol{B}_d^T \left(\int_{\Omega_e} \boldsymbol{C}_t d\boldsymbol{\varepsilon}_d d\Omega\right) d\Omega = \frac{1}{\Omega_e}\left(\int_{\Omega_e} \boldsymbol{B}_d^T d\Omega\right) \cdot \left(\int_{\Omega_e} \boldsymbol{C}_t d\boldsymbol{\varepsilon}_d d\Omega\right) = 0. \tag{67}$$

Finally, with $d\bar{\boldsymbol{\varepsilon}} = \frac{1}{\Omega_e}\boldsymbol{L} d\boldsymbol{u}$ and $d\boldsymbol{\varepsilon}_d = \boldsymbol{B}_d d\boldsymbol{u}$, adding (64) and (66) and considering (67), we obtain

$$\boldsymbol{K}_T \equiv \frac{1}{\Omega_e}\boldsymbol{L}\bar{\boldsymbol{C}}_t\boldsymbol{L}^T + \int_{\Omega_e} \boldsymbol{B}_d^T \boldsymbol{C}_t \boldsymbol{B}_d d\Omega + \frac{1}{\Omega_e}\int_{\Omega_e} (\boldsymbol{L}\boldsymbol{C}_t\boldsymbol{B}_d + \boldsymbol{B}_d^T\boldsymbol{C}_t\boldsymbol{L}^T) d\Omega - \frac{1}{\Omega_e}\int_{\Omega_e} \boldsymbol{B}_d^T \bar{\boldsymbol{C}}_t \boldsymbol{L}^T d\Omega. \tag{68}$$

The expression (68) can be further simplified: again using (61), and noting that $\boldsymbol{L}$ and $\bar{\boldsymbol{C}}_t$ are constant, the last term of $\boldsymbol{K}_T$ is null:

$$\int_{\Omega_e} \boldsymbol{B}_d^T \bar{\boldsymbol{C}}_t \boldsymbol{L}^T d\Omega = \left(\int_{\Omega_e} \boldsymbol{B}_d^T d\Omega\right) \cdot \bar{\boldsymbol{C}}_t \boldsymbol{L}^T = 0 \tag{69}$$

thus,

$$\boldsymbol{K}_T \equiv \frac{1}{\Omega_e}\boldsymbol{L}\bar{\boldsymbol{C}}_t\boldsymbol{L}^T + \int_{\Omega_e} \boldsymbol{B}_d^T \boldsymbol{C}_t \boldsymbol{B}_d d\Omega + \frac{1}{\Omega_e}\int_{\Omega_e} (\boldsymbol{L}\boldsymbol{C}_t\boldsymbol{B}_d + \boldsymbol{B}_d^T\boldsymbol{C}_t\boldsymbol{L}^T) d\Omega. \tag{70}$$

If one assumes that $\boldsymbol{C}_t$ is symmetric (either "naturally" symmetric if derived from an associative plasticity model, or "artificially" symmetrized if from an non-associative plasticity model), the last term of $\boldsymbol{K}_T$ can be viewed as the symmetric part of $\boldsymbol{L}\boldsymbol{C}_t\boldsymbol{B}_d$:

$$\boldsymbol{C}_t \text{ symmetric } : \boldsymbol{C}_t = \boldsymbol{C}_t^T \Rightarrow \boldsymbol{L}\boldsymbol{C}_t\boldsymbol{B}_d + \boldsymbol{B}_d^T\boldsymbol{C}_t\boldsymbol{L}^T = 2[\boldsymbol{L}\boldsymbol{C}_t\boldsymbol{B}_d]_{\text{Sym}},$$

where $[\square]_{\text{Sym}}$ is the symmetric part of $\square$, i.e. $[\square]_{\text{Sym}} \equiv \frac{1}{2}(\square + \square^T)$. So assuming $\boldsymbol{C}_t$ symmetric, the final expression of $\boldsymbol{K}_T$ reduces to

$$\boldsymbol{K}_T \equiv \frac{1}{\Omega_e}\boldsymbol{L}\bar{\boldsymbol{C}}_t\boldsymbol{L}^T + \int_{\Omega_e} \boldsymbol{B}_d^T \boldsymbol{C}_t \boldsymbol{B}_d d\Omega + \frac{2}{\Omega_e}\int_{\Omega_e} [\boldsymbol{L}\boldsymbol{C}_t\boldsymbol{B}_d]_{\text{Sym}} d\Omega. \tag{71}$$

Since it has been considered in this work the associated rule (plastic flow normal to the yield surface), $\boldsymbol{C}_t$ is symmetric and Eq. (71) has been used forward.

The last term of $\boldsymbol{K}_T$ is a coupling term between the low and high order deformation modes due to the (possibly) non-uniformity of the tangent constitutive operator $\boldsymbol{C}_t$ in the element domain Ω_e.

Note that if the element is "fully elastic", this coupling term is null (i.e. $\overline{\boldsymbol{C}}_t = \boldsymbol{C}_t = \boldsymbol{C}_e$, the elastic constitutive operator, and $\int_{\Omega_e} \boldsymbol{B}_d d\Omega = 0$): for example noting that $\boldsymbol{L}$ and $\boldsymbol{C}_e$ are constant, the coupling term $\int_{\Omega_e} \boldsymbol{L}\boldsymbol{C}_e\boldsymbol{B}_d d\Omega$ simplifies to

$$\int_{\Omega_e} \boldsymbol{L}\boldsymbol{C}_e\boldsymbol{B}_d d\Omega = \boldsymbol{L}\boldsymbol{C}_e \cdot \left(\int_{\Omega_e} \boldsymbol{B}_d d\Omega \right) = 0$$

and the same for $\int_{\Omega_e} \boldsymbol{B}_d^T \boldsymbol{C}_e \boldsymbol{L}^T d\Omega$. We then recover the standard ANDES stiffness splitting into low and high order contributions. Note that this is a consequence of the "energy orthogonality" constrain between the low and high order strain deformation modes.

Remark.

(1) The definition of $\boldsymbol{F}_{int,H}$ in (58) uses the "deviatoric" stress $\boldsymbol{\sigma}_d$. But thanks to the property $\int_{\Omega_e} \boldsymbol{B}_d d\Omega = 0$, $\boldsymbol{F}_{int,H}$ can be directly computed in term of $\boldsymbol{\sigma}$:

$$\begin{aligned} \boldsymbol{F}_{int,H} &\equiv \int_{\Omega_e} \boldsymbol{B}_d^T \boldsymbol{\sigma}_d d\Omega = \int_{\Omega_e} \boldsymbol{B}_d^T \boldsymbol{\sigma} d\Omega - \left(\int_{\Omega_e} \boldsymbol{B}_d^T d\Omega \right) \cdot \bar{\boldsymbol{\sigma}} \\ &= \int_{\Omega_e} \boldsymbol{B}_d^T \boldsymbol{\sigma} d\Omega. \end{aligned} \tag{72}$$

Infact, $\boldsymbol{B}_d^T$ filters out the constant component $\bar{\boldsymbol{\sigma}}$ of $\boldsymbol{\sigma}$. This just shows that the splitting of $\boldsymbol{F}_{int}$ into *low or basis* ($\boldsymbol{F}_{int,B}$) and *high* ($\boldsymbol{F}_{int,H}$) order contributions in (58) is completely consistent from the implementation point of view

$$\begin{aligned} \boldsymbol{F}_{int} &\equiv \boldsymbol{F}_{int,B} + \boldsymbol{F}_{int,H} = \boldsymbol{L}\bar{\boldsymbol{\sigma}} + \int_{\Omega_e} \boldsymbol{B}_d^T \boldsymbol{\sigma} d\Omega \\ &= \int_{\Omega_e} \left(\frac{1}{\Omega_e} \boldsymbol{L}^T + \boldsymbol{B}_d \right)^T \boldsymbol{\sigma} d\Omega, \end{aligned} \tag{73}$$

which is nothing than the standard expression of $\boldsymbol{F}_{int}$:

$$\boldsymbol{F}_{int} \equiv \int_{\Omega_e} B^T \boldsymbol{\sigma} d\Omega, \text{ with } B \equiv \frac{1}{\Omega_e} \boldsymbol{L}^T + \boldsymbol{B}_d \tag{74}$$

and thus

$$\boldsymbol{K}_T \equiv \int_{\Omega_e} B^T \boldsymbol{C}_t B d\Omega \tag{75}$$

Consequently this splitting is quite artificial, but it was mainly done in this work to follow the ANDES framework. Note that taking advantage of this splitting can produce a better implementation (less flops needed: no need to explicit build B) and provide a better understanding of the coupling term in the stiffness matrix.

(2) The introduction of the scaling factor β of the high order contribution (from the ANDES framework) can be easily done by replacing each instance of $\boldsymbol{B}_d$ by $\sqrt{\beta}\boldsymbol{B}_d$. Doing so, one will obtain

$$\boldsymbol{F}_{int} = \boldsymbol{L}\bar{\boldsymbol{\sigma}} + \sqrt{\beta} \int_{\Omega_e} \boldsymbol{B}_d^T \boldsymbol{\sigma}_d d\Omega, \tag{76}$$

$$\boldsymbol{K}_T = \frac{1}{\Omega_e} \boldsymbol{L}\overline{\boldsymbol{C}}_t \boldsymbol{L}^T + \beta \int_{\Omega_e} \boldsymbol{B}_d^T \boldsymbol{C}_t \boldsymbol{B}_d d\Omega + \frac{2\sqrt{\beta}}{\Omega_e} \int_{\Omega_e} [\boldsymbol{L}\boldsymbol{C}_t \boldsymbol{B}_d]_{\text{Sym}} d\Omega. \tag{77}$$

Note that in this case B is equal to $\frac{1}{\Omega_e}\boldsymbol{L}^T + \sqrt{\beta}\boldsymbol{B}_d$.

(3) The vector $\boldsymbol{v}$ is being used in this section to represent the deformational part of the total displacements vector.

4.2.2. Elastoplastic ANDES element following the classical plate/shell theories

As usual in classical plate/shell theories (see [36]), the position vector $\boldsymbol{X}$ (in a global frame) of a point in a plate/shell element is parameterized by

$$\boldsymbol{x} \equiv (\eta, \xi), \quad \boldsymbol{X} = \boldsymbol{x} + z \cdot \boldsymbol{n}(\boldsymbol{x}), \tag{78}$$

where $\boldsymbol{x}$ is the position vector of an associated point on the plate/shell mid-surface, $\boldsymbol{n}(\boldsymbol{x})$ is the normal to the plate/shell mid-surface, and z is the coordinate along thickness of the element in the local frame. Let $\boldsymbol{\Upsilon}$ and $\boldsymbol{\Sigma}$ be the plate/shell (generalized) "strains" and "stress":

$$\boldsymbol{\Upsilon} \equiv \{\boldsymbol{e}, \boldsymbol{\chi}\}, \quad \boldsymbol{\Sigma} \equiv \{N, M\} \tag{79}$$

where $\boldsymbol{e}$ and $\boldsymbol{\chi}$ are the extensional and bending/curvature part of the plate/shell "strains", and N, M are the associated static quantities, i.e. stress resultant and moment. Note that all these quantities are only function of the area coordinates:

$$\boldsymbol{\Upsilon} = \boldsymbol{\Upsilon}(\boldsymbol{x}), \quad \boldsymbol{\Sigma} = \boldsymbol{\Sigma}(\boldsymbol{x}). \tag{80}$$

They are constant throughout of thickness of the plate/shell (see classical plate/shell theories). Anyway, we can easily compute *local* 3D classical strains $\boldsymbol{\varepsilon}$ from plate/shell "strains" as (for classical models):

$$\boldsymbol{\varepsilon}(\boldsymbol{X}) = \boldsymbol{\varepsilon}(\boldsymbol{x}, z) \equiv \boldsymbol{e}(\boldsymbol{x}) + z \cdot \boldsymbol{\chi}(\boldsymbol{x}) \tag{81}$$

and compute plate/shell "stresses" from *local* 3D/plane stress classical stresses by integrating the local stress field $\boldsymbol{\sigma}$ through of thickness:

$$N(\boldsymbol{x}) \equiv \int_h \boldsymbol{\sigma}(\boldsymbol{X}) dz, \quad M(\boldsymbol{x}) \equiv \int_h z \cdot \boldsymbol{\sigma}(\boldsymbol{X}) dz, \quad \boldsymbol{\sigma}(\boldsymbol{X}) = \boldsymbol{\sigma}(\boldsymbol{x}, z). \tag{82}$$

Following the same way, from the *local plane stress* elastic and tangent constitutive operator,

$$\boldsymbol{\sigma} = \boldsymbol{C}_e \boldsymbol{\varepsilon}, \quad d\boldsymbol{\sigma} = \boldsymbol{C}_t d\boldsymbol{\varepsilon} \tag{83}$$

one can obtain plate/shell-like elastic and tangent constitutive operators:

$$\boldsymbol{\Sigma} = \boldsymbol{D}_e \boldsymbol{\Upsilon}, \quad d\boldsymbol{\Sigma} = \boldsymbol{D}_t d\boldsymbol{\Upsilon}. \tag{84}$$

In general case (excluding shear effect), $\boldsymbol{D}_\bullet$ ($\boldsymbol{D}_e$ or $\boldsymbol{D}_t$) has the following structure:

$$\boldsymbol{D}_\bullet = \begin{bmatrix} \boldsymbol{D}_\bullet^m & \boldsymbol{D}_\bullet^{mb} \\ \boldsymbol{D}_\bullet^{bm} & \boldsymbol{D}_\bullet^b \end{bmatrix}, \quad \boldsymbol{D}_\bullet^{bm} = \boldsymbol{D}_\bullet^{mb}, \tag{85}$$

where $\boldsymbol{D}_\bullet^m$ and $\boldsymbol{D}_\bullet^b$ are the membrane and bending elastic/tangent constitutive operators, and $\boldsymbol{D}_\bullet^{mb}$ is the coupling membrane-bending term. This terms are obtained by integrating $\boldsymbol{C}_\bullet$ ($\boldsymbol{C}_e$ or $\boldsymbol{C}_t$) through of thickness:

$$\begin{aligned} \boldsymbol{D}_\bullet^m(\boldsymbol{x}) &\equiv \int_h \boldsymbol{C}_\bullet(\boldsymbol{x}, z) dz, \\ \boldsymbol{D}_\bullet^b(\boldsymbol{x}) &\equiv \int_h z^2 \cdot \boldsymbol{C}_\bullet(\boldsymbol{x}, z) dz, \\ \boldsymbol{D}_\bullet^{mb}(\boldsymbol{x}) = \boldsymbol{D}_\bullet^{bm}(\boldsymbol{x}) &\equiv \int_h z \cdot \boldsymbol{C}_\bullet(\boldsymbol{x}, z) dz. \end{aligned} \tag{86}$$

In particular case of isotropic elasticity, one recovers the standard expression of $\boldsymbol{D}_e^m$ and $\boldsymbol{D}_e^b$:

$$\boldsymbol{D}_e^m \equiv \int_h \boldsymbol{C}_e dz = h\boldsymbol{C}_e, \quad \boldsymbol{D}_e^b \equiv \int_h z^2 \cdot \boldsymbol{C}_e dz = \frac{h^3}{12} \boldsymbol{C}_e, \quad \boldsymbol{D}_e^{mb} = \boldsymbol{D}_e^{bm} = 0. \tag{87}$$

In a Finite Element framework, plate/shell (generalized) "strains" can be obtained from the elementary vector of freedom degrees $\boldsymbol{v}$ by using the formulation/element dependant strain–displacement operator:

$$\boldsymbol{\Upsilon}(\boldsymbol{x}) = B(\boldsymbol{x})\boldsymbol{v} = \left(\frac{1}{A_e} \boldsymbol{L}^T + \sqrt{\beta} \boldsymbol{B}_d(\boldsymbol{x}) \right) \boldsymbol{v}. \tag{88}$$

4.2.3. Internal force vector proposed by this work

Following the ANDES Finite Element framework, the elementary internal force vector is computed from the plate/shell "stresses" $\boldsymbol{\Sigma}$ as:

$$\boldsymbol{F}_{int} \equiv \boldsymbol{F}_{int,B} + \boldsymbol{F}_{int,H} = \boldsymbol{L}\bar{\boldsymbol{\Sigma}}_e + \sqrt{\beta}\int_{A_e} \boldsymbol{B}_d^T \boldsymbol{\Sigma}_d dA, \tag{89}$$

where

$$\bar{\boldsymbol{\Sigma}}_e \equiv \frac{1}{A_e}\int_{A_e} \boldsymbol{\Sigma} dA, \boldsymbol{\Sigma}_d \equiv \boldsymbol{\Sigma} - \bar{\boldsymbol{\Sigma}}_e$$

and A_e represents the area of the element.

But if one considers the following relations:

$$\boldsymbol{\Sigma}_e = (N, M), \quad N = \int_h \boldsymbol{\sigma} dz, \quad M = \int_h z\boldsymbol{\sigma} dz, \tag{90}$$

$$\bar{\boldsymbol{\Sigma}}_e = (\overline{N}, \overline{M}), \quad \overline{N} = \frac{1}{A_e}\int_{Ae} N dA, \quad \overline{M} = \frac{1}{A_e}\int_{Ae} zM dA, \tag{91}$$

$$\boldsymbol{L} = \begin{bmatrix} \boldsymbol{L}^m & 0 \\ 0 & \boldsymbol{L}^b \end{bmatrix}, \quad \boldsymbol{B}_d = \begin{bmatrix} \boldsymbol{B}_d^m & 0 \\ 0 & \boldsymbol{B}_d^b \end{bmatrix} \tag{92}$$

then Eq. (89) can be written as

$$\boldsymbol{F}_{int} = \begin{bmatrix} \boldsymbol{L}^m & 0 \\ 0 & \boldsymbol{L}^b \end{bmatrix} \begin{bmatrix} \overline{N} \\ \overline{M} \end{bmatrix} + \sqrt{\beta}\int_{Ae} \begin{bmatrix} \boldsymbol{B}_d^m & 0 \\ 0 & \boldsymbol{B}_d^b \end{bmatrix}^T \begin{bmatrix} N - \overline{N} \\ M - \overline{M} \end{bmatrix} dA. \tag{93}$$

4.2.4. Material tangent stiffness proposed by this work

Assuming $\boldsymbol{D}_t$ symmetric, the (consistent) tangent stiffness matrix $\boldsymbol{K}_T$ is given by

$$\boldsymbol{K}_T \equiv \frac{1}{A_e}\boldsymbol{L}\overline{\boldsymbol{D}}_t\boldsymbol{L}^T + \beta\int_{A_e} \boldsymbol{B}_d^T \boldsymbol{D}_t \boldsymbol{B}_d dA + \frac{2\sqrt{\beta}}{A_e}\int_{A_e} [\boldsymbol{L}\boldsymbol{D}_t\boldsymbol{B}_d]_{\mathrm{Sym}} dA \tag{94}$$

with

$$\boldsymbol{L} = \text{constant}, \quad \boldsymbol{B}_d = \boldsymbol{B}_d(\boldsymbol{x}), \quad \boldsymbol{D}_t = \boldsymbol{D}_t(\boldsymbol{x}), \quad \overline{\boldsymbol{D}}_t \equiv \frac{1}{A_e}\int_{A_e} \boldsymbol{D}_t dA.$$

Remark. The last term of Eq. (94) is the new parcel introduced by this work in the material tangent stiffness of the ANDES element. As shown in the previous section, this term is null in the case of the linear elastic analysis, because the tangent operator is constant and Eq. (61) can be applied.

Once more, if one consider Eq. (92) and the following one: $\boldsymbol{D}_t = \begin{bmatrix} \boldsymbol{D}_t^m & \boldsymbol{D}_t^{mb} \\ \boldsymbol{D}_t^{bm} & \boldsymbol{D}_t^b \end{bmatrix}$; then, each parcel of Eq. (94) can be written as follows:

$$\boldsymbol{L}\overline{\boldsymbol{D}}_t\boldsymbol{L}^T = \boldsymbol{L}^m\overline{\boldsymbol{D}}_t^m\boldsymbol{L}^{mT} + \boldsymbol{L}^b\overline{\boldsymbol{D}}_t^b\boldsymbol{L}^{bT} + \boldsymbol{L}^m\overline{\boldsymbol{D}}_t^{mb}\boldsymbol{L}^{bT} + \boldsymbol{L}^b\overline{\boldsymbol{D}}_t^{bm}\boldsymbol{L}^{mT}, \tag{95}$$

$$\beta\int_{A_e} \boldsymbol{B}_d^T\boldsymbol{D}_t\boldsymbol{B}_d dA = \beta^m\int_{A_e} \boldsymbol{B}_d^{mT}\boldsymbol{D}_t^m\boldsymbol{B}_d^m dA + \beta^b\int_{A_e} \boldsymbol{B}_d^{bT}\boldsymbol{D}_t^b\boldsymbol{B}_d^b dA + \sqrt{\beta^m\beta^b}\int_{A_e} \boldsymbol{B}_d^{mT}\boldsymbol{D}_t^{mb}\boldsymbol{B}_d^b dA + \sqrt{\beta^b\beta^m}\int_{A_e} \boldsymbol{B}_d^{bT}\boldsymbol{D}_t^{bm}\boldsymbol{B}_d^m dA, \tag{96}$$

$$\frac{2\sqrt{\beta}}{A_e}\int_{A_e} [\boldsymbol{L}\boldsymbol{D}_t\boldsymbol{B}_d]_{\mathrm{Sym}} dA = \frac{2\sqrt{\beta^m}}{A_e}\int_{A_e} [\boldsymbol{L}^m\boldsymbol{D}_t^m\boldsymbol{B}_d^m]_{\mathrm{Sym}} dA + \frac{2\sqrt{\beta^b}}{A_e} \times \int_{A_e} [\boldsymbol{L}^b\boldsymbol{D}_t^b\boldsymbol{B}_d^b]_{\mathrm{Sym}} dA + \frac{2\sqrt{\beta^{mb}}}{A_e} \times \int_{A_e} [\boldsymbol{L}^m\boldsymbol{D}_t^{mb}\boldsymbol{B}_d^b]_{\mathrm{Sym}} dA + \frac{2\sqrt{\beta^{bm}}}{A_e} \times \int_{A_e} [\boldsymbol{L}^b\boldsymbol{D}_t^{bm}\boldsymbol{B}_d^m]_{\mathrm{Sym}} dA. \tag{97}$$

After algebraic manipulations, Eqs. (95)–(97) become

$$\boldsymbol{K}_T = \boldsymbol{K}_T^m + \boldsymbol{K}_T^b + \boldsymbol{K}_T^{mb} + \boldsymbol{K}_T^{bm}, \tag{98}$$

where

$$\boldsymbol{K}_T^m = \boldsymbol{L}^m\overline{\boldsymbol{D}}_t^m\boldsymbol{L}^{mT} + \beta^m\int_{A_e} \boldsymbol{B}_d^{mT}\boldsymbol{D}_t^m\boldsymbol{B}_d^m dA + \frac{2\sqrt{\beta^m}}{A_e}\int_{A_e} [\boldsymbol{L}^m\boldsymbol{D}_t^m\boldsymbol{B}_d^m]_{\mathrm{Sym}}, \tag{99}$$

$$\boldsymbol{K}_T^b = \boldsymbol{L}^b\overline{\boldsymbol{D}}_t^b\boldsymbol{L}^{bT} + \beta^b\int_{A_e} \boldsymbol{B}_d^{bT}\boldsymbol{D}_t^b\boldsymbol{B}_d^b dA + \frac{2\sqrt{\beta^b}}{A_e}\int_{A_e} [\boldsymbol{L}^b\boldsymbol{D}_t^b\boldsymbol{B}_d^b]_{\mathrm{Sym}}, \tag{100}$$

$$\boldsymbol{K}_T^{mb} = \boldsymbol{L}^m\overline{\boldsymbol{D}}_t^{mb}\boldsymbol{L}^{bT} + \sqrt{\beta^m\beta^b}\int_{A_e} \boldsymbol{B}_d^{mT}\boldsymbol{D}_t^{mb}\boldsymbol{B}_d^b dA + \frac{2\sqrt{\beta^{mb}}}{A_e}\int_{A_e} [\boldsymbol{L}^m\boldsymbol{D}_t^{mb}\boldsymbol{B}_d^b]_{\mathrm{Sym}} dA, \tag{101}$$

$$\boldsymbol{K}_T^{bm} = \boldsymbol{L}^b\overline{\boldsymbol{D}}_t^{bm}\boldsymbol{L}^{mT} + \sqrt{\beta^b\beta^m}\int_{A_e} \boldsymbol{B}_d^{bT}\boldsymbol{D}_t^{bm}\boldsymbol{B}_d^m dA + \frac{2\sqrt{\beta^{bm}}}{A_e}\int_{A_e} [\boldsymbol{L}^b\boldsymbol{D}_t^{bm}\boldsymbol{B}_d^m]_{\mathrm{Sym}} dA. \tag{102}$$

As one can see in Eq. (98), the last two parcels are membrane/bending coupling terms. Furthermore, the low/high order coupling terms are present in all parcels in Eq. (98), like it is shown in Eqs. (99)–(102).

Still Eq. (98) can be written in matrix form:

$$\boldsymbol{K}_T = \begin{bmatrix} \boldsymbol{L}^m & 0 \\ 0 & \boldsymbol{L}^b \end{bmatrix} \begin{bmatrix} \overline{\boldsymbol{D}}_t^m & \overline{\boldsymbol{D}}_t^{mb} \\ \overline{\boldsymbol{D}}_t^{bm} & \overline{\boldsymbol{D}}_t^b \end{bmatrix} \begin{bmatrix} \boldsymbol{L}^m & 0 \\ 0 & \boldsymbol{L}^b \end{bmatrix}^T + \begin{bmatrix} \boldsymbol{B}_d^m & 0 \\ 0 & \boldsymbol{B}_d^b \end{bmatrix} \begin{bmatrix} \beta^m\boldsymbol{D}_t^m & \sqrt{\beta^m\beta^b}\boldsymbol{D}_t^{mb} \\ \sqrt{\beta^b\beta^m}\boldsymbol{D}_t^{bm} & \beta^b\boldsymbol{D}_t^b \end{bmatrix} \begin{bmatrix} \boldsymbol{B}_d^m & 0 \\ 0 & \boldsymbol{B}_d^b \end{bmatrix}^T + \begin{bmatrix} \boldsymbol{L}^m & 0 \\ 0 & \boldsymbol{L}^b \end{bmatrix} \begin{bmatrix} \frac{2\sqrt{\beta^m}}{Ae}\boldsymbol{D}_t^m & \frac{2\sqrt{\beta^m\beta^b}}{Ae}\boldsymbol{D}_t^{mb} \\ \frac{2\sqrt{\beta^b\beta^m}}{Ae}\boldsymbol{D}_t^{bm} & \frac{2\sqrt{\beta^b}}{Ae}\boldsymbol{D}_t^b \end{bmatrix} \begin{bmatrix} \boldsymbol{B}_d^m & 0 \\ 0 & \boldsymbol{B}_d^b \end{bmatrix} \tag{103}$$

The last term of Eq. (103) was first introduced by this work, and it accounts for the coupling term between basic and high order stiffness. It was considered also in Eq. (103) the coupling term between membrane and bending strains. Both coupling terms listed above have an important influence in the algorithm's convergence rate. If one performs the isotropic elastic analysis (without composite materials – for the case of the membrane/bending coupling term), both coupling term vanish and the standard stiffness of the ANDES element (Eq. 57) is recovered.

At this point the internal force vector and the full material tangent stiffness matrix (for the elastoplastic ANDES element) are ready to be implemented.

5. Numerical examples

Some numerical examples are analyzed below in order to evaluate the performance of the ANDES element, when it is subjected to the co-rotational and elastoplastic formulations, as they are suggested in this work. The results shown herein are concerned to aspects like convergence of the algorithm, variation of the number of Gauss points through of thickness of the element, and mesh variation. Examples from the literature are used in order to compare the answers (see references [18,37,38]).

5.1. Perfectly plastic analysis of a simply supported plate under punctual load

A perfectly plastic analysis of a simply supported plate under a punctual load on its center has been performed in this example, either to emphasize the new terms of the tangent matrix and to verify the influence of the number of Gauss points and the refinement of the meshes in the analysis. The layer approach has been used herein as plastic model. The plate has been analyzed for 3, 5 and 7 Gauss points through of thickness and 3 Gauss points over the area of the element. This example consider the meshes with $10 \times 10 \times 2$, $15 \times 15 \times 2$ and $20 \times 20 \times 2$ triangular ANDES elements. The closer to the applied load, the more discretized were the meshes. The numerical simulation was performed with a quarter of the plate because of its symmetry. The convergence tolerance was 1.0×10^{-10} for the arch-length iteration (either residual load norm, displacements norm or energy norm) and also for the plastic iterations. The geometrical and physically features of the plate are (Fig. 3): square plate (16 m $\times$ 16 m), $h = 0.5$ m, $\nu = 0.2$, $E = 7.05 \times 10^6$ N/mm^2, $\sigma_Y = 2.44 \times 10^2$ N/mm^2, $K = 0.0$.

Fig. 4 shows that for a single mesh, as more Gauss points through of thickness has the element, as closer to convergence is the algorithm. Also, if the number of Gauss points remain constant, the mesh refinement does not give significant change in the path equilibrium. Possibly in this case a much higher discretization of the mesh would be necessary to get closer to convergence. Otherwise, the main difference occurs when the number of Gauss points changes from 3 to 5. This means that 5 Gauss points through of thickness are already enough to achieve a good approximation, and nothing more than $15 \times 15 \times 2$ elements are needed, once a finer mesh would not give significantly differences in results, in this case. Hence, the mesh with $15 \times 15 \times 2$ elements and 5 Gauss points through of thickness have been used for the results listed in Tables 1 and 2.

In order to emphasize the new terms of the tangent matrix, as they were shown in Eq. (94), Tables 1 and 2 show the convergence (residual norm) of the algorithm either for full material tangent stiffness, without the membrane/bending coupling terms, without the low/high order coupling terms or without both coupling terms listed above (standard ANDES element). The algorithm was run for the symmetric and unsymmetric cases. The mesh used in this test was $15 \times 15 \times 2$ triangular elements and it has been used 5 Gauss point through of thickness of the element. Table 1 was constructed with the results of the step 24 ($\lambda \approx 0.29961, U_Z \approx -7.6383 \times 10^{-3}$), and Table 2 with the results of the step 92 ($\lambda \approx 0.6416, U_Z \approx -6.0007 \times 10^{-2}$).

Table 1 shows that the full material tangent stiffness (standard ANDES formulation + membrane/bending coupling terms + low/high order coupling terms) reaches the convergence already at

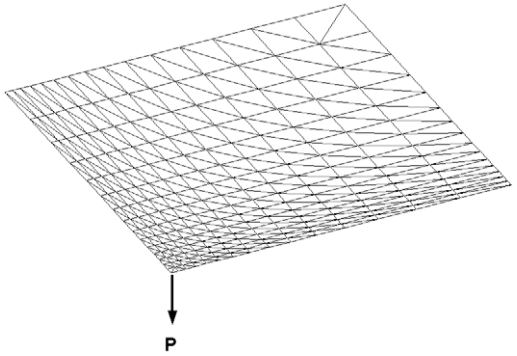

Fig. 3. Undeformed configuration of the plate.

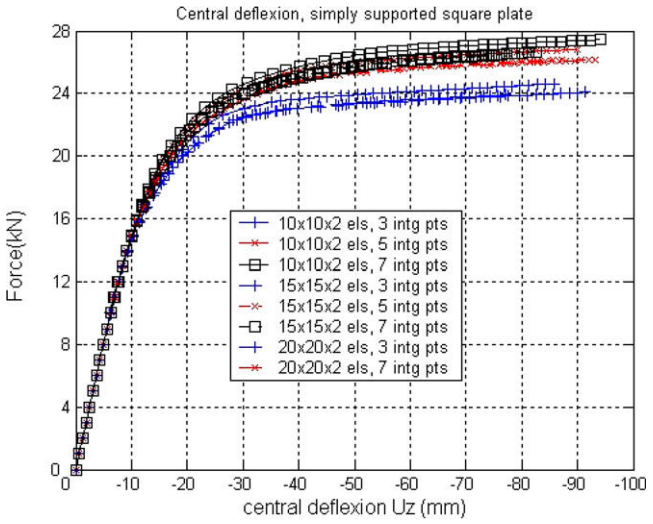

Fig. 4. Path equilibrium of the plate.

Table 1
Convergence results of the plate at the 24th step.

Solver	Unsymmetric	Symmetric	Symmetric	Symmetric	Symmetric
$\boldsymbol{K}_T^m$	Complete	Complete	Complete	$\boldsymbol{K}_b^m + \boldsymbol{K}_h^m$	$\boldsymbol{K}_b^m + \boldsymbol{K}_h^m$
$\boldsymbol{K}_T^b$	Complete	Complete	Complete	$\boldsymbol{K}_b^b + \boldsymbol{K}_h^b$	$\boldsymbol{K}_b^b + \boldsymbol{K}_h^b$
$\boldsymbol{K}_T^{mb}$	Complete	Complete	–	$\boldsymbol{K}_b^{mb} + \boldsymbol{K}_h^{mb}$	–
$\boldsymbol{K}_T^{bm}$	Complete	Complete	–	$\boldsymbol{K}_b^{bm} + \boldsymbol{K}_h^{bm}$	–
Iterations	$\|R\|$	$\|R\|$	$\|R\|$	$\|R\|$	$\|R\|$
1	2.39e+01	1.95e+01	3.32e+00	3.58e+00	3.69e+00
2	9.61e+00	8.44e+00	6.68e+00	1.16e+01	4.12e+00
3	1.09e+00	1.00e+00	3.53e−01	1.03e+00	9.93e−01
4	2.85e−02	2.16e−02	1.44e−03	2.95e+00	1.01e+00
5	3.43e−05	1.60e−05	4.51e−05	2.47e−01	1.57e−01
6	–	–	2.00e−05	4.80e−01	1.80e−01
7	–	–	1.80e−06	1.58e−01	5.92e−02
8	–	–	–	1.08e−01	3.23e−02
9	–	–	–	6.29e−02	3.10e−02
10	–	–	–	2.97e−02	1.17e−02
11	–	–	–	2.31e−02	1.25e−02
12	–	–	–	9.04e−03	5.03e−03
13	–	–	–	7.82e−03	4.43e−03
14	–	–	–	2.96e−03	1.94e−03
15	–	–	–	2.52e−03	1.47e−03
16	–	–	–	9.94e−04	6.95e−04
17	–	–	–	7.89e−04	4.66e−04
18	–	–	–	3.36e−04	2.41e−04
19	–	–	–	2.43e−04	1.45e−04
20	–	–	–	1.14e−04	8.25e−05
21	–	–	–	–	4.44e−05
22	–	–	–	–	2.84e−05

Table 2
Convergence results of the plate at the 92th step.

Solver	Unsymmetric	Symmetric	Symmetric	Symmetric	Symmetric
$\boldsymbol{K}_T^m$	Complete	Complete	Complete	$\boldsymbol{K}_b^m + \boldsymbol{K}_h^m$	$\boldsymbol{K}_b^m + \boldsymbol{K}_h^m$
$\boldsymbol{K}_T^b$	Complete	Complete	Complete	$\boldsymbol{K}_b^b + \boldsymbol{K}_h^b$	$\boldsymbol{K}_b^b + \boldsymbol{K}_h^b$
$\boldsymbol{K}_T^{mb}$	Complete	Complete	–	$\boldsymbol{K}_b^{mb} + \boldsymbol{K}_h^{mb}$	–
$\boldsymbol{K}_T^{bm}$	Complete	Complete	–	$\boldsymbol{K}_b^{bm} + \boldsymbol{K}_h^{bm}$	–
Iterations	$\|R\|$	$\|R\|$	$\|R\|$	$\|R\|$	$\|R\|$
1	6.41e+01	4.03e+01	6.97e+00	Div step 27	Div step 27
2	4.30e+01	3.13e+01	5.16e+00	–	–
3	1.09e+00	2.58e+00	3.50e−01	–	–
4	5.09e−01	1.81e−01	2.91e−03	–	–
5	4.13e−03	5.03e−04	6.56e−05	–	–
6	9.39e−07	8.98e−07	7.75e−06	–	–
7	–	–	1.05e−06	–	–
8	–	–	1.14e−06	–	–

the fifth iteration, either with symmetric or with unsymmetric solver. When the membrane/bending coupling term is off, the convergence still is good, but two more iterations are necessary. When the low/high order coupling term is off, 15 more iterations are necessary. Using only the standard ANDES formulation, the algorithm needs seventeenth more iterations to reach the convergence. In this case (simply supported plate), the membrane/bending coupling term does not have significant influence in the convergence of the algorithm, because the bending efforts prevail over the plate. At the step 24, 1102 integrations points had reached plasticity, which means 8.4% over the domain. The convergence rate of the algorithm is linear when the low/high order coupling terms are not used, but it becomes quadratic when they are used.

Table 2 shows that if the low/high order coupling term is not used, the algorithm diverges at the step 27. Also, at the step 92 the convergence rate is still quadratic and no more than six iterations are needed to the algorithm reaches the convergence, in the full stiffness case. The membrane/bending term continues insignificant in this case. At this step, 9.712 integrations points had reached plasticity, which means 74.4% of the domain.

5.2. Perfectly plastic analysis of a Scordelis roof under distributed load

In this example an perfectly plastic analysis of the Scordelis roof under distributed load over its surface has been performed. As plastic model the layer approach has been used. The roof has been analyzed for 5 Gauss points through of thickness and 3 Gauss points over the area of the element. The meshes used were $10 \times 10 \times 2$ and $16 \times 16 \times 2$ triangular ANDES elements and the numerical simulation was performed with a quarter of the roof because of its symmetry. The boundary conditions can be seen in Fig. 5, where circles means support nodes, squares means x–z symmetry nodes and diamond means y–z symmetry nodes.

The convergence tolerance was 1.0×10^{-10} for the arch-length iteration (either residual load norm, displacements norm or energy norm) and also for the plastic iterations. The geometrical and physically features and the material properties of the element are: $h = 76$ mm, $\nu = 0.0$, $E = 2.1 \times 10^4$ N/mm^2, $\sigma_Y = 4.2$ N/mm^2, $K = 0.0$, $F_0 = 4.0$ kN/ mm^2, *length* $= 15.2$ m, *radius* $= 7.6$ m (from center of curvature), $\theta = 80^\circ$ (between the edge sides).

The integration of the stress through of thickness of the element, which is the subject of this work, gives more accurate results than stress resultant analysis (as performed by Skallerud and Haugen [18]), if one considers Brank [38] as reference, which accounts even the shear effect - thick shell/plate (see Fig. 6). Also, a refinement of the mesh gives more accurate results. Fig. 7 shows the deformed mesh of the Scordelis roof after the last load step.

5.3. Linear isotropic elastoplastic analysis of a pinched cylinder under punctual loads

In this example a linear isotropic elastoplastic analysis of a pinched cylinder under two diametral opposite loads has been performed. As plastic model the layer approach has been used. The cylinder has been analyzed for 5 Gauss points through of thickness and 3 Gauss points over the area of the element. The meshes used were $20 \times 20 \times 2$ and $30 \times 30 \times 2$ triangular ANDES elements and the numerical simulation was performed with an eighth of the cylinder because of its symmetry. The boundary conditions can be seen in Fig. 8, where circles means diaphragm nodes, squares means x–y symmetry nodes, diamond means y–z symmetry nodes and triangle means x–z symmetry nodes.

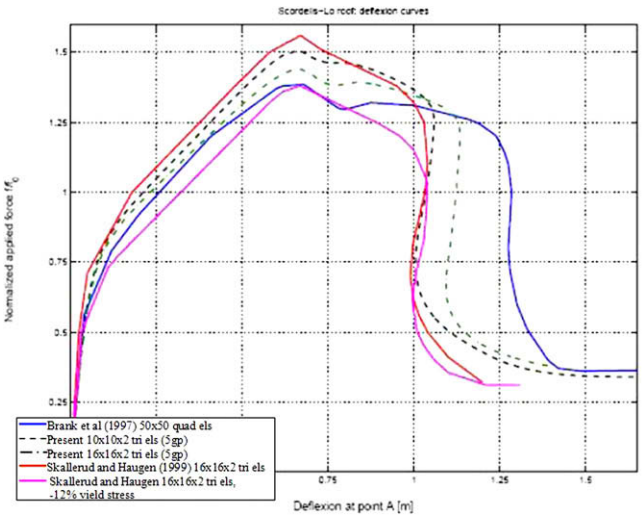

Fig. 6. Path equilibrium of the Scordelis roof.

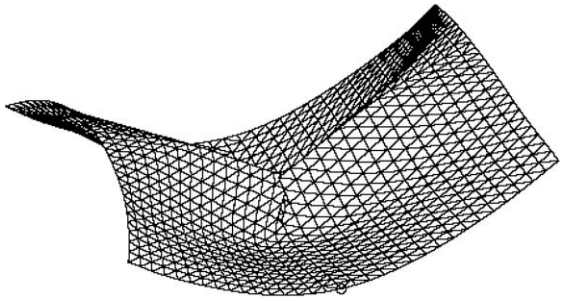

Fig. 7. Deformed configuration of the Scordelils roof.

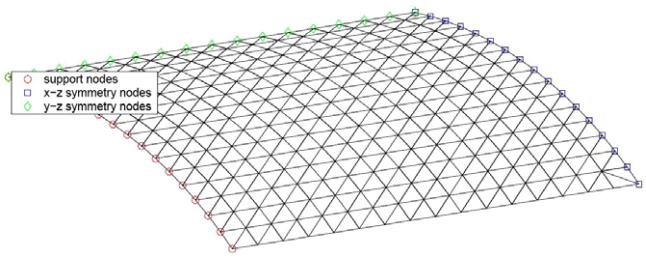

Fig. 5. Undeformed configuration of Scordelis roof.

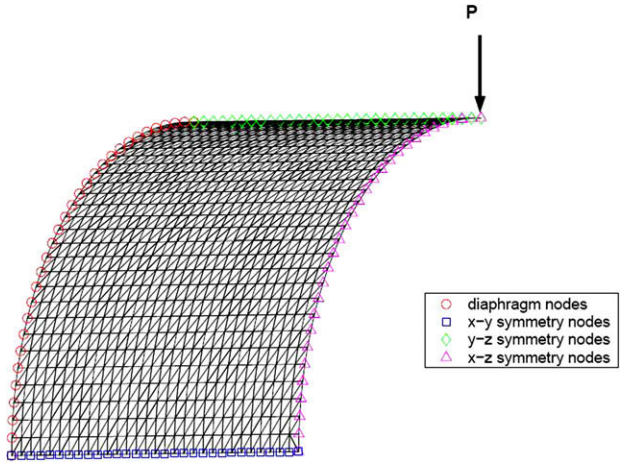

Fig. 8. Undeformed configuration of pinched cylinder.

The convergence tolerance was 1.0×10^{-10} for the arch-length iterations (either residual load norm, displacements norm or energy norm) and also for the plastic iterations. The geometrical and physically features and the material properties of the element are shown below: $h = 3.0$ mm, $\nu = 0.3$, $E = 3.0 \times 10^3$ Mpa, $\sigma_Y = 24.3$ Mpa, $K = 5.0 \times 10^1$, *lenght* $= 300$ mm, *radius* $= 300$ mm.

Again, integration of the stress through of thickness of the element, which is the subject of this work, gives more accurate results than stress resultant analysis, obtained by Skallerud and Haugen [18], if the reference is Brank et al. [38], which considers even the shear effect – thick shell/plate (see Fig. 9). In this case, by using the mesh $20 \times 20 \times 2$ (present work) one can see the appearance of local buckles on the path equilibrium. But a refinement of the mesh gives a more accurate result, as is the case of the $30 \times 30 \times 2$ mesh (present work). Fig. 10 shows the deformed state of the pinched cylinder, after the last load step.

In order to emphasize the influence of the tangent stiffness contributions on the non-linear convergence history, Table 3 shows the convergence results at step 10 ($\lambda \approx 1.67210^2$ and $u_z \approx -3.946010^1$), for every cases considered in the previous convergence tables. The triangular ANDES element mesh was made with $30 \times 30 \times 2$ elements. At this point, 375 integrations points were already in the plastic domain ($\approx 1.4\%$ of the integrations points were in the plastic domain).

Table 3 shows that for the pinched cylinder analysis, the full unsymmetric material tangent stiffness gives the best result in term of convergence at the step 10. The full symmetric matrix still gives a good convergence at this step. But, the tangent stiffness without membrane/bending coupling term needs 25 iterations at the 10th step to reach the convergence, and the tangent stiffness without low/high order coupling term needs 17 iterations at the same step to reach the convergence. This means that in this case the membrane/bending coupling term has more importance than the low/high order coupling term, but both of them operate significative changes in the convergence rate. The standard ANDES element needs 33 steps to achieve the convergence.

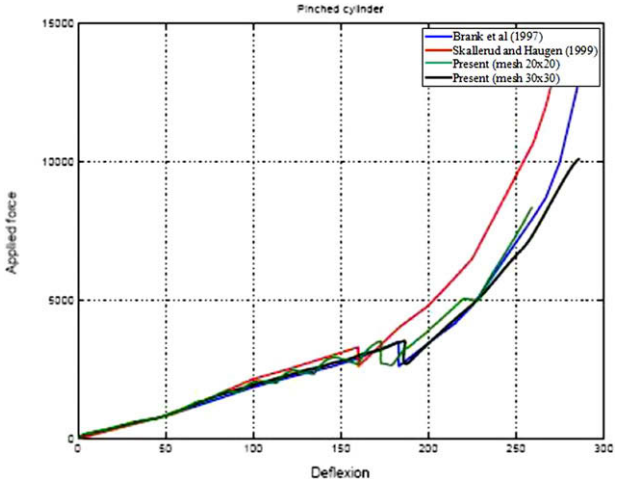

Fig. 9. Path equilibrium of the pinched cylinder.

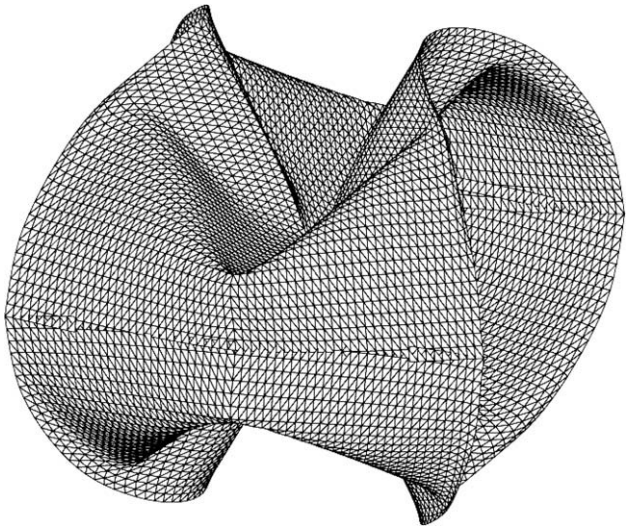

Fig. 10. Deformed configuration of the pinched cylinder.

5.4. Buckling linear-exponential isotropic elastoplastic analysis of a clamped cylinder under axial load

In this example a linear-exponential isotropic elastoplastic analysis of a clamped cylinder under axial loads has been performed, where the following exponential isotropic hardening function was implemented: $R(p) = \sigma_Y + Kp + Q_1(1 - e^{-b_1 p}) + Q_2(1 - e^{-b_2 p})$. As plastic model the layer approach has been used. The cylinder has been analyzed for 5 Gauss points through of thickness and 3 Gauss points over the area of the element. The meshes used were $20 \times 30 \times 2$ triangular ANDES elements and the numerical simulation was performed with a eighth of the cylinder because of its symmetry.

Table 3
Convergence results of the pinched cylinder at the 10th step.

Solver	Unsymmetric	Symmetric	Symmetric	Symmetric	Symmetric
$\boldsymbol{K}_T^m$	Complete	Complete	Complete	$\boldsymbol{K}_b^m + \boldsymbol{K}_h^m$	$\boldsymbol{K}_b^m + \boldsymbol{K}_h^m$
$\boldsymbol{K}_T^b$	Complete	Complete	Complete	$\boldsymbol{K}_b^b + \boldsymbol{K}_h^b$	$\boldsymbol{K}_b^b + \boldsymbol{K}_h^b$
$\boldsymbol{K}_T^{mb}$	Complete	Complete	–	$\boldsymbol{K}_b^{mb} + \boldsymbol{K}_h^{mb}$	–
$\boldsymbol{K}_T^{bm}$	Complete	Complete	–	$\boldsymbol{K}_b^{bm} + \boldsymbol{K}_h^{bm}$	–
Iterations	$\|R\|$	$\|R\|$	$\|R\|$	$\|R\|$	$\|R\|$
1	1.19e+01	1.67e+01	1.60e+01	1.67e+01	1.60e+01
2	5.09e+00	9.10e+00	5.23e+00	8.90e+00	5.31e+00
3	3.64e−01	8.11e−01	1.41e+01	6.61e−01	1.52e+00
4	5.51e−03	7.61e−02	1.97e−01	1.40e−01	2.20e−01
5	1.05e−06	6.29e−04	4.10e−02	2.52e−02	6.72e−02
6	2.32e−10	2.52e−05	2.13e−02	7.09e−03	3.40e−02
7	–	1.90e−06	5.44e−03	1.82e−03	1.15e−02
8	–	8.53e−08	2.55e−03	5.19e−04	6.18e−03
9	–	6.45e−09	6.92e−04	1.39e−04	2.52e−03
10	–	3.79e−10	3.11e−04	3.94e−05	1.35e−03
11	–	–	9.14e−05	1.09e−05	6.58e−04
12	–	–	4.04e−05	3.09e−06	3.59e−04
13	–	–	1.37e−05	8.72e−07	1.94e−04
14	–	–	6.19e−06	2.48e−07	1.08e−04
15	–	–	2.56e−06	7.09e−08	6.08e−05
16	–	–	1.25e−06	2.03e−08	3.45e−05
17	–	–	5.76e−07	5.84e−09	1.96e−05
18	–	–	2.83e−07	–	1.12e−05
19	–	–	1.42e−07	–	6.39e−06
20	–	–	7.10e−08	–	3.65e−06
21	–	–	3.60e−08	–	2.09e−06
22	–	–	1.82e−08	–	1.20e−06
23	–	–	9.26e−09	–	6.86e−07
24	–	–	4.70e−09	–	3.93e−07
25	–	–	2.40e−09	–	2.25e−07
26	–	–	–	–	1.29e−07
27	–	–	–	–	7.38e−08
28	–	–	–	–	4.23e−08
29	–	–	–	–	2.42e−08
30	–	–	–	–	1.39e−08
31	–	–	–	–	7.95e−09
32	–	–	–	–	4.56e−09
33	–	–	–	–	2.62e−09

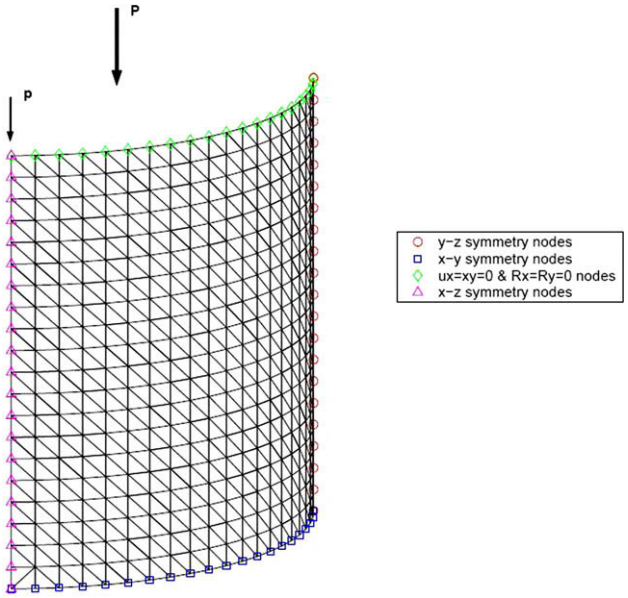

Fig. 11. Undeformed configuration of clamped cylinder.

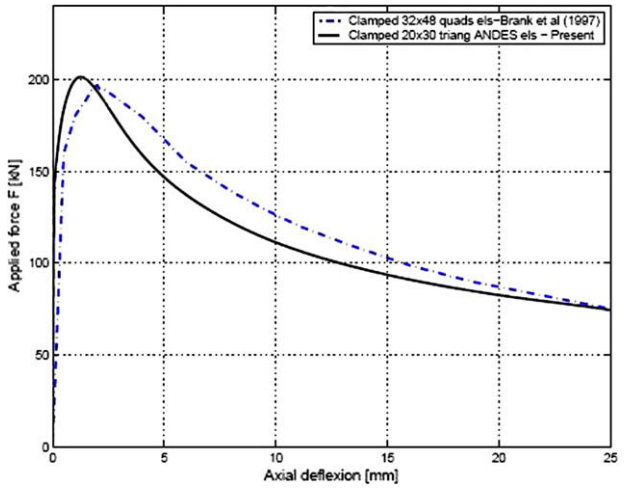

Fig. 12. Path equilibrium of the clamped cylinder.

The boundary conditions can be seen in Fig. 11, where diamonds means displacements $v_x = 0$ and $v_y = 0$, rotations $R_x = 0$ and $R_y = 0$, circles means y–z symmetry nodes, squares means x–y symmetry nodes and triangle means x–z symmetry nodes. The convergence tolerance was 1.0×10^{-10} for the arch-length iteration (either residual load norm, displacements norm or energy norm) and also for the plastic iterations. The geometrical and physically features and the material properties of the element are shown below: $h = 2.36$ mm, $v = 0.274$, $E = 2.16962 \times 10^5$ Mpa, $\sigma_Y = 162.722$ Mpa, $K = 1290.2697$, $Q_1 = 85.56$ Mpa, $b_1 = 183.3645$, $Q_2 = 52.8282$ Mpa, $b_2 = 10394.7903$, *length* = 127.1 mm, *radius* = 2.36 mm.

Fig. 12 shows the good agreement of the present work in relation to the Branks' curve. Brank et al. [38] have obtained results for a thick shell/plate, which accounted even the shear effect. Like one can see in this reference, the results are compared with available experimental results and representative numerical simulations.

Fig. 13 shows the evolution of the deformed configuration and the plastic strain over the surface of the cylinder (see the showing up of the two rings symmetrically close to the ends of the cylinder).

5.5. Linear-exponential isotropic elastoplastic analysis of the V22 stiffened wing panel

This example is an application of the formulation proposed in this work in a real case. It has been performed herein a linear-exponential isotropic elastoplastic analysis for the V22 stiffened wing panel (which belongs to V22 Osprey helicopter) under axial loads, where the linear-exponential isotropic hardening function which has been used is: $R(p) = \sigma_Y + Kp + Q_1(1 - e^{-b_1 p}) + Q_2(1 - e^{-b_2 p})$. The layer approach has been used herein as plastic model and all coupling terms of stiffness matrix have been considered. The panel has been analyzed for 5 Gauss points through of thickness and 3 Gauss points over the area of the element. The mesh used was 9136 triangular ANDES elements. The numerical simulation was performed with a half of the object because of its symmetry. Other geometrical features can bee seen in Fig. 14.

The convergence tolerance was 1.0×10^{-10} for the arch-length iteration (either residual load norm, displacements norm or energy norm) and also for the plastic iterations. The panel is made with 2 different materials, which are: aluminium ($v = 0.36$, $E = 6.9 \times 10^4$ Mpa, $\sigma_Y = 305$ Mpa, $K = 454.45$, $Q_1 = 16.287$ Mpa, $b_1 = 592.0$, $Q_2 = 133.285$ Mpa, $b_2 = 16.30$) and steel ($v = 0.3$, $E = 2.07 \times 10^5$ Mpa, $\sigma_Y = 1.0 \times 10^{10}$ Mpa, $K = 0.0$, $Q_1 = 0.0$ Mpa, $b_1 = 0.0$, $Q_2 = 0.0$ Mpa, $b_2 = 0.0$). There are 22 different thin shell element thickness over the panel. The axial load (-1.5×10^6 kN) was applied on the middle node at the end of the panel, but it was equally distributed through of panel width by the rigid coupling nodes. The total projection area of the panel is 1930.4×889.0 mm^2. The stiffness of the panel is largely increased by the longitudinal beams disposed over its area.

Fig. 15 shows the equilibrium path of the point A (see this point in Fig. 16), in V22 wing panel, for the elastic and elastoplastic cases.

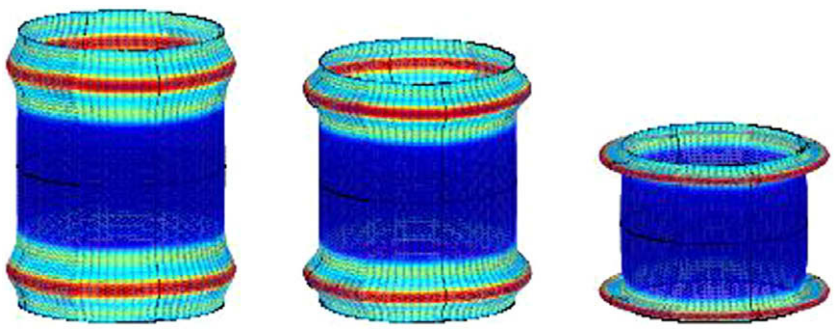

Fig. 13. Evolution of the plastic strain of the clamped cylinder.

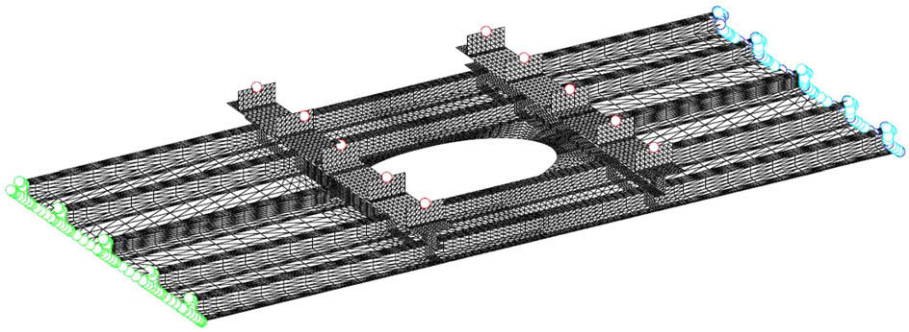

Fig. 14. Undeformed configuration of the V22 wing panel.

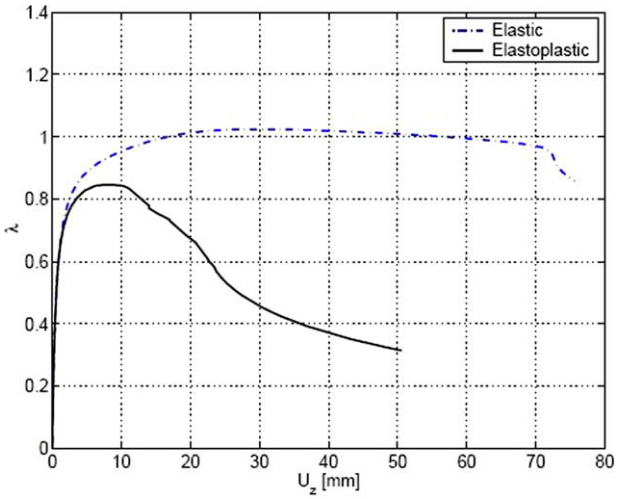

Fig. 15. Vertical deflexion of point A on the V22 wing panel.

Fig. 16 shows the deformed configuration over the body of V22 wing panel, and Fig. 17 shows its plastic strain.

6. Concluding remarks

The goal of this work was to perform the geometrically and physically non-linearity analysis for thin shell structures by using the CSSE co-rotational formulation, the ANDES thin shell element, and Simo's plasticity formulation. In order to achieve this goal, it became necessary to create a new way to obtain the internal force vector and the tangent stiffness matrix for the ANDES thin shell finite element. As a consequence of this development, the ANDES thin shell element became more general, because it now accounts for the coupling term between low- and high order stiffness and the coupling terms between membrane and bending strains. At the end of the present investigation, one may conclude the following: (1) the integration of the stresses through of element's thickness and the consideration of the coupling terms (membrane/bending strains – low/high order stiffness) provide more accurate results than those obtained from the stress resultant analysis, because the first one allows a better description of the plasticity in the shell thickness; (2) in cases where there exists prevalence of membrane efforts over bending efforts or vice-versa, the membrane/bending coupling term of the tangent stiffness scarcely interferes on the convergence rate (see numerical example 5.1). (3) Depending on the case to be analyzed, the low/high order stiffness coupling term has more importance in certain situations while the membrane/bending coupling term has more importance in others. However, as regards the cases analyzed by the present work, the full tangent stiffness always provides the best results in terms of convergence. If one uses the unsymmetrical solver, the results may be even better. (4) The mesh exerts influence on the results; (5) this study revealed that at least 5 Gauss points are required through of thickness of the element in order to capture the plastic strain distribution; (6) the benchmarks in the literature are generally in good agreement with the present work; (7) from the results obtained thus far, it seems that the combined co-rotational and elastoplastic formulations are attractive because a substantial amount of the existing co-rotational formulation can be reused, with the elastoplastic behaviour representing an additional capability implementation. Such simplicity is achieved at the cost of assuming a small strain behaviour.

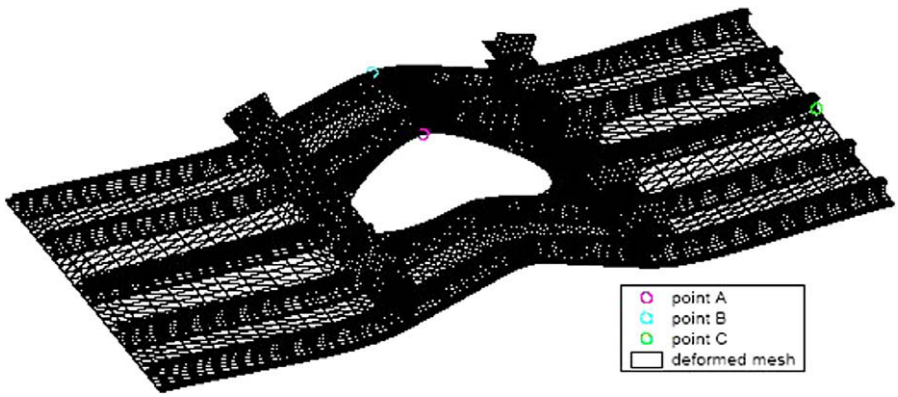

Fig. 16. Deformed configuration of the V22 wing panel.

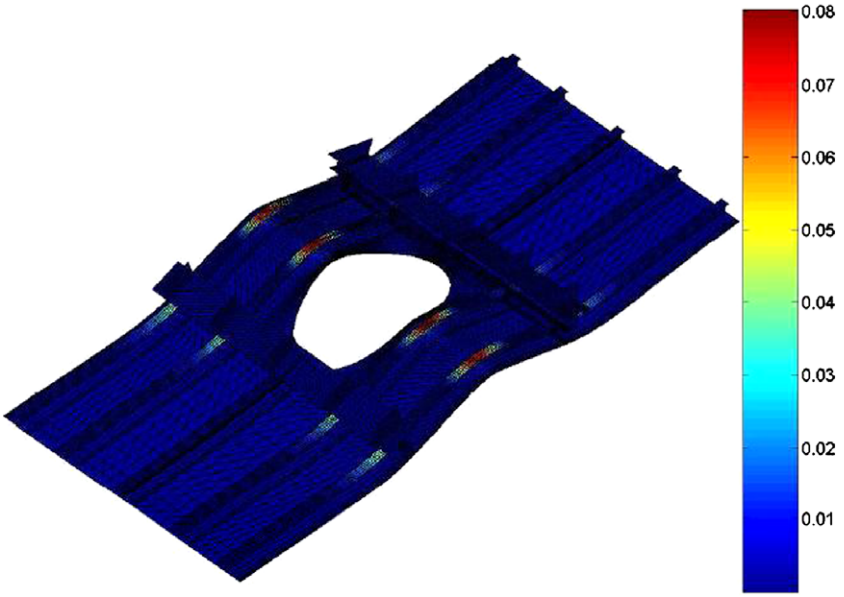

Fig. 17. Plastic strain of the V22 wing panel.

Acknowledgements

Funded by Universidade do Estado de Santa Catarina – UDESC and Coordenação de Aperfeiçoamento de Pessoal de Nível Superior – CAPES.

References

[1] G.A. Wempner, Finite elements, finite rotations and small strains of flexible shells, Int. J. Sol. Struct. 5 (1969) 117–153.
[2] T. Belytschko, B.J. Hsieh, Non-linear transient finite element analysis with convected coordinates, Int. J. Numer. Methods Engrg. 7 (1973) 255–271.
[3] B.M. Fraeijis de veubeke, The dynamics of flexible bodies, Int. J. Engrg. Sci. (1976) 895–913.
[4] P.G. Bergan, M.K. Nygard, Nonlinear shell analysis using free formulation finite elements, in finite element methods for nonlinear problems, Int. J. Numer. Methods Engrg. (1989) 317–388.
[5] M.K. Nygard, The free formulation for nonlinear finite element with application to shells, Ph.D. thesis, Div. of Structural Mechanics, Norwegian Institute of Technology, Trondheim, Norway, 1986.
[6] C.C. Rankin, E.A. Brogan, An element-independent corotational procedure for the treatment of large rotations, ASME J. Pressure Vessel Technol. 108 (1986) 165–174.
[7] B. Nour-omid, C.C. Rankin, Finite rotation analysis and consistent linearization using projectors, Comput. Methods Appl. Mech. Engrg. 93 (1991) 353–384.
[8] C.C. Rankin, B. Nour-omid, The use of projectors to improve finite element performance, Comput. Struct. 30 (1988) 257–267.
[9] P.G. Bergan, M.K. Nygard, Finite elements with increased freedom in choosing shape functions, Int. J. Numer. Methods Engrg. 20 (1984) 643–664.
[10] B. Haugen, Buckling and stability problems for thin shell structures using high performance finite elements, Ph.D. thesis, University of Colorado, EUA, 1994.
[11] C.A. Felippa, B. Haugen, A unified formulation of small-strain corotational finile elements: I. Theory, Comput. Methods Appl. Mech. Engrg. 194 (2005) 2285–2335.
[12] J.M. Battini, A modified corotational framework for triangular shell elements, Comput. Methods Appl. Mech. Engrg. 196 (2007) 1905–1914.
[13] J.C. Simo, T.J.R. Hughes, Computational inelasticity, Interdisciplinary Applied Mathematics, vol. 7, Springer, 1998.
[14] I. Doltsinis, Elements of Plasticity, Theory and Computation, WIT press, 2000.
[15] A. Pérez-foguet, F. Armero, On the formulation of closest-point projection algorithms in elastoplasticity – part I: the variational structure, Int. J. Numer. Methods Engrg. 53 (2002) 297–329.
[16] M.A. Save, C.E. Massonnet, G. Saxce, Plastic Limit Analysis of Plates, Shells and Disks, Elsevier, 1997.
[17] A. Ibrahimbegovic, Stress resultant geometrically exact shell theory for finite rotations and its finite element implementation, Appl. Mach. Rev. 50 (1997) 199–226.
[18] B. Skallerud, B. Haugen, Collapse of thin shell structures – stress resultant plasticity modelling within a co-rotated ANDES finite element formulation, Int. J. Numer. Methods Engrg. 46 (1999) 1961–1986.
[19] N.D. Cortivo, Plastic buckling and collapse of thin shell structures, using corotational, layered plastic model and ANDES finite element formulations, Ph.D. thesis, University of Brasilia, Brasil, 2004.
[20] J.M. Battini, C. Pacoste, On the choice of the linear element for corotational triangular shells, Comput. Methods Appl. Mech. Engrg. 195 (2006) 6362–6377.
[21] Y.B. Yang, S.P. Lin, C.S. Chen, Rigid body concept for geometric nonlinear analysis of 3d frames, plates and shells based on updated lagrangian formulation, Comput. Methods Appl. Mech. Engrg. 196 (2007) 1178–1192.
[22] C.A. Felippa, C. Militello, Membrane triangles with corner drilling freedoms. II. The ANDES element, Finite Elem. Anal. 12 (1992) 189–201.
[23] M.A. Crisfield, Non-linear Finite Element Analysis of Solids and Structures, vol. 36, Springer, 1997.
[24] J.H. Argyris, An excursion into large rotations, Comput. Methods Appl. Mech. Engrg. 32 (1985) 85–155.
[25] A. Cardona, An integrated approach to mechanism analysis, Ph.D. thesis, University of Liege, Belgium, 1989.
[26] W.F. Chen, H. Zhang, Structural Plasticity, Theory, Problems, and CAE Software, Springer, 1990.
[27] A. Pérez-foguet, F. Armero, On the formulation of closest-point projection algorithms in elastoplasticity – part II: globally convergent schemes, Int. J. Numer. Methods Engrg. 53 (2002) 331–374.
[28] C. Militello, C.A. Felippa, The first ANDES elements: 9-dof plate bending triangles, Comput. Methods Appl. Mech. Engrg. 93 (1991) 217–246.
[29] C.A. Felippa, Parametrized multifield variational principles in elasticity: I. mixed functionals, Commun. Appl. Numer. Methods 5 (1989) 79–88.
[30] C.A. Felippa, Parametrized multifield variational principles in elasticity: II. Hybrid functionals and free formulation, Commun. Appl. Numer. Methods 5 (1989) 89–98.
[31] C.A. Felippa, A survey of parametrized variational principles and applications to computational mechanics, Comput. Methods Appl. Mech. Engrg. 113 (1994) 109–139.
[32] C.A. Fellipa, B. Haugen, C. Militello, From the individual element test to finite element templates: Evolution of the patch test, Int. J. Numer. Methods Engrg. 38 (1995) 199–229.
[33] C. Militello, Application on parametrized variational principles to the finite element method, Ph.D. dissertation, Department of Aeroespace Engineering Sciences, University of Colorado, EUA, 1991.
[34] C.A. Felippa, S. Alexander, Membrane triangles with corner drilling freedoms. III. Implementation and performance evaluation, Finite Elem. Anal. 12 (1992) 203–239.
[35] P.G. Bergan, L. Hanssen, A new approach for deriving "good finite elements, Math. Finite Elem. Appl. 2 (1976) 483–497.
[36] E. O-ate, Calculation of Structures by Finite Element Method, Linear Static Analysis, Artes Graficas Torres, SA, 1992.
[37] J.C. Simo, J.G. Kennedy, On stress resultant geometrically exact shell model: part V. Nonlinear plasticity, Comput. Methods Appl. Mech. Engrg. 96 (1992) 133–171.
[38] B. Brank, D. Peric, F. Damjanic, On large deformations of thin elasto-plastic shells: implementation of a finite rotation model for quadrilateral shell element, Int. J. Numer. Methods Engrg. 40 (1997) 689–726.